IMA Journal of Applied Mathematics (2021) **00**, 1–28
https://doi.org/10.1093/imamat/hxab025

Downloaded from https://academic.oup.com/imamat/advance-article/doi/10.1093/imamat/hxab025/6318163 by University of California, Berkeley user on 12 July 2021

Localized states in passive and active phase-field-crystal models

Max Philipp Holl*
Institut für Theoretische Physik, Westfälische Wilhelms-Universität Münster, Wilhelm-Klemm-Str. 9, 48149 Münster, Germany
*Corresponding author: m.p.holl@wwu.de

Andrew J. Archer
Department of Mathematical Sciences, Loughborough University, Loughborough, Leicestershire, LE11 3TU, UK
Interdisciplinary Centre for Mathematical Modelling, Loughborough University, Loughborough, Leicestershire, LE11 3TU, UK

Svetlana V. Gurevich
Institut für Theoretische Physik, Westfälische Wilhelms-Universität Münster, Wilhelm-Klemm-Str. 9, 48149 Münster, Germany
Center for Nonlinear Science (CeNoS), Westfälische Wilhelms-Universität Münster, Corrensstr. 2, 48149 Münster, Germany

Edgar Knobloch
Department of Physics, University of California, Berkeley, California 94720, USA

Lukas Ophaus
Institut für Theoretische Physik, Westfälische Wilhelms-Universität Münster, Wilhelm-Klemm-Str. 9, 48149 Münster, Germany

and

Uwe Thiele
Institut für Theoretische Physik, Westfälische Wilhelms-Universität Münster, Wilhelm-Klemm-Str. 9, 48149 Münster, Germany
Center for Nonlinear Science (CeNoS), Westfälische Wilhelms-Universität Münster, Corrensstr. 2, 48149 Münster, Germany

[Received on 02 October 2020; revised on 25 May 2021; accepted on 10 June 2021]

The passive conserved Swift–Hohenberg equation (or phase-field-crystal [PFC] model) describes gradient dynamics of a single-order parameter field related to density. It provides a simple microscopic description of the thermodynamic transition between liquid and crystalline states. In addition to spatially extended periodic structures, the model describes a large variety of steady spatially localized structures. In appropriate bifurcation diagrams the corresponding solution branches exhibit characteristic slanted homoclinic snaking. In an active PFC model, encoding for instance the active motion of self-propelled colloidal particles, the gradient dynamics structure is broken by a coupling between density and an additional polarization field. Then, resting and traveling localized states are found with transitions characterized by parity-breaking drift bifurcations. Here, we briefly review the snaking behavior of localized states in passive and active PFC models before discussing the bifurcation behavior of localized states in systems of (i) two coupled passive PFC models with common gradient dynamics, (ii) two coupled

© The Author(s) 2021. Published by Oxford University Press on behalf of the Institute of Mathematics and its Applications. All rights reserved.

passive PFC models where the coupling breaks the gradient dynamics structure and (iii) a passive PFC model coupled to an active PFC model.

Keywords: localized states; homoclinic slanted snaking; active phase field crystal; bifurcation analysis; numerical continuation.

1. Introduction

Phenomena involving pattern formation are widespread in nature and are also encountered in technologically relevant processes (Ball, 1999). Strictly speaking, by 'pattern formation', one refers to the self-organized emergence[1] of spatially periodic (or quasiperiodic) structures that can be steady or, more generally, exhibit temporally regular dynamics (Cross & Greenside, 2009; Cross & Hohenberg, 1993; Hoyle, 2006; Pismen, 2006). Often, the underlying processes are described by continuum models, i.e. the patterns correspond to solutions of partial differential equations. Over the years much attention has focused on infinitely extended patterns as well as on domain-filling patterns in finite domains with prescribed boundary conditions (Cross & Hohenberg, 1993). However, it was also found that under certain conditions finite pattern patches may coexist with an infinitely extended uniform background (or a background formed by a different pattern). Such structures are the localized states that are the subject of the present volume. Examples include the localized buckling of a long beam under compression (Hunt *et al.*, 2000), localized patches of traveling waves in binary mixture convection (Barten *et al.*, 1991; Surko *et al.*, 1991), dissipative solitons in bistable optical systems (Tlidi *et al.*, 1994), bound states of oscillons in vibrated layers of sand (Umbanhowar *et al.*, 1996) and patches of peaks close to the onset of the Rosensweig instability of the free surface of a magnetic fluid (Lloyd *et al.*, 2015).

Localized states have been extensively investigated for many individual physical systems like those mentioned above. Remarkably, these share a number of common features that are independent of the particular physics involved. In bifurcation diagrams that present the various localized states that arise as a function of a control parameter, the branches of localized states of different types often form a snakes-and-ladders structure referred to as 'homoclinic snaking' (Burke & Knobloch, 2006; Woods & Champneys, 1999).

Localized states are frequently described by means of generic equations from the theory of pattern formation, particularly the Swift-Hohenberg (SH) equation and its variants (Burke & Knobloch, 2006, 2007; Hilali *et al.*, 1995; Sakaguchi & Brand, 1996). This equation can be written as

$$\partial_t \phi = -M \frac{\delta \mathscr{F}_{\mathrm{sh}}[\phi]}{\delta \phi}, \tag{1.1}$$

where M is a positive mobility constant. This variational form highlights the fact that the SH equation describes gradient dynamics of an order parameter field ϕ with the underlying energy functional

$$\mathscr{F}_{\mathrm{sh}}[\phi] \equiv \int_V \mathrm{d}^n\mathbf{r} \left[f(\phi) - q^2(\nabla\phi)^2 + \frac{1}{2}(\Delta\phi)^2 \right]. \tag{1.2}$$

Since equation (1.1) does not preserve the 'mass' $\int_V \phi \, \mathrm{d}^n\mathbf{r}$, it represents 'nonconserved dynamics'.

[1] Here, we use 'self-organization' in a loose sense but acknowledge that its precise meaning, exact relation to dissipative processes and discrimination from (dynamic) self-assembly are widely and wildly discussed issues.

Downloaded from https://academic.oup.com/imamat/advance-article/doi/10.1093/imamat/hxab025/6318163 by University of California, Berkeley user on 12 July 2021

The local energy $f(\phi)$ is typically a double-well potential such as $f = f_{24} \equiv (r+q^2)\phi^2/2 + \phi^4/4$ (Cross & Hohenberg, 1993), or $f = f_{234} \equiv (r+q^2)\phi^2/2 - b_3\phi^3/3 + \phi^4/4$ (Burke & Knobloch, 2006; Hilali *et al.*, 1995).[2] More complicated forms like $f = f_{246} \equiv (r+q^2)\phi^2/2 - b_4\phi^4/4 + \phi^6/6$ (Avitabile *et al.*, 2010; Burke & Knobloch, 2007; Houghton & Knobloch, 2011; Sakaguchi & Brand, 1996) and a quadratic-quartic-sextic-octic potential (Knobloch *et al.*, 2019) have also been investigated. Snaking localized states are found in all of the mentioned examples except f_{24} and have been investigated in one (Houghton & Knobloch, 2011), two (Avitabile *et al.*, 2010; Lloyd & Sandstede, 2009; Lloyd *et al.*, 2008; McCalla & Sandstede, 2010) and three dimensions (McCalla & Sandstede, 2010). The influence of various nonvariational modifications of Eq. (1.1) through additional terms that break its gradient structure has also been discussed (Bordeu *et al.*, 2016; Burke & Dawes, 2012; Burke *et al.*, 2009; Hariz *et al.*, 2019; Houghton & Knobloch, 2011; Kozyreff & Tlidi, 2007; Kubstrup *et al.*, 1996; Lejeune *et al.*, 2004).

The simple potential f_{24} does not allow for localized states because the primary bifurcation is always supercritical and, in consequence, the trivial uniform state $\phi = 0$ and the spatially periodic patterned state do not exist as linearly stable states at identical parameter values. Such coexistence is a condition for localized states to occur in systems with nonconserved dynamics. The resulting localized states exhibit aligned or 'vertical' snaking where like saddle-node bifurcations all occur asymptotically at the same parameter value (Burke & Knobloch, 2006, 2007).

In contrast to the SH equation (1.1), the conserved SH equation (Thiele *et al.*, 2013) does conserve mass. This equation is prominent in material science as the 'phase-field-crystal (PFC) model' (Elder & Grant, 2004; Emmerich *et al.*, 2012) and is sometimes called the derivative SH equation (Cox, 2004; Matthews & Cox, 2000). It takes the form

$$\partial_t \phi = M\Delta \frac{\delta \mathscr{F}_{\mathrm{sh}}[\phi]}{\delta \phi} \tag{1.3}$$

with the energy functional again given by Eq. (1.2). In this case the local energy $f(\phi)$ can be taken to be the simplest double-well potential f_{24} since this time it does allow for the coexistence of homogeneous and patterned states even when the primary bifurcation is supercritical. However, because of mass conservation, the coexisting states typically represent different mean concentrations (Thiele *et al.*, 2013). In effect, the overall mean density $\bar{\phi}$ takes the role of the parameter b_3 in f_{234} in the standard SH equation.

One finds that the localized states again form a homoclinic snaking structure, although this time it is no longer vertically aligned but slanted (Thiele *et al.*, 2013). Such slanted snaking is also observed in other pattern-forming systems with a conservation law (Dawes, 2008; Knobloch, 2015; Lo Jacono *et al.*, 2011; Pradenas *et al.*, 2017). Ultimately, the tilting of the snakes-and-ladders structure is due to the finite domain size as expulsion [absorption] of mass from [into] the expanding localized pattern implies an increase [decrease] of the mean density in the uniform background. This progressively changes the value of the control parameter where the next peak of the pattern forms. As a result, localized states exist in a larger parameter range than in nonconserved systems. Slanted snaking may also appear in systems with spatial periodic heterogeneity (Bortolozzo *et al.*, 2008) and be induced by certain boundary conditions (Kozyreff *et al.*, 2009).

[2] Note that different sign conventions for the parameter r are in use.

Downloaded from https://academic.oup.com/imamat/advance-article/doi/10.1093/imamat/hxab025/6318163 by University of California, Berkeley user on 12 July 2021

In the conserved SH equation and related PFC models, slanted snaking is observed when the mean density or the effective temperature r are used as the primary control parameter (Robbins *et al.*, 2012; Thiele *et al.*, 2013). However, it takes the form of standard aligned snaking when the bifurcation diagram is plotted as a function of the chemical potential. This is because the natural control parameter for conserved dynamics is the mean density while controlling the chemical potential corresponds to nonconserved dynamics (see the conclusions in Thiele *et al.*, 2013, and Engelnkemper *et al.*, 2019). The localization of patterns due to a conserved quantity is also considered by Cox & Matthews (2003) for a nonvariational extension of the PFC model. There, in the nomenclature of Engelnkemper *et al.* (2019), a nonvariational chemical potential and an additional nonvariational flux are added to the conserved SH equation.

In a major extension the PFC model may be combined with elements of the Toner–Tu theory for self-propelled particles (Toner & Tu, 1995) to obtain an active PFC model as a description of crystallization-like nonequilibrium transitions in systems of active colloidal particles (Menzel & Löwen, 2013). In this approach the density field is coupled to a new field, the polarization field. The coupling, quantified by an 'activity parameter', breaks the gradient dynamics structure of the PFC model thereby allowing for sustained motion and states that oscillate in time. Note that nonvariational modifications of the standard SH equation may also result in traveling states (Burke & Dawes, 2012; Houghton & Knobloch, 2011; Kozyreff & Tlidi, 2007) although with quite different onset behavior.

The active PFC model is one of many models developed to capture collective phenomena, like motility-induced clustering and swarm formation in active hydrodynamic and soft matter systems (Marchetti *et al.*, 2013). It shows transitions between a liquid state and an extended patterned (crystalline) state, as well as transitions between resting and traveling patterns (Chervanyov *et al.*, 2016; Menzel & Löwen, 2013; Menzel *et al.*, 2014). Experimentally, related resting (Thar & Kühl, 2005) or traveling (Bechinger *et al.*, 2016; Ginot *et al.*, 2018; Palacci *et al.*, 2013; Petroff *et al.*, 2015; Theurkauff *et al.*, 2012) patches of particles with nearly crystalline order (Toner *et al.*, 2005) are reported as 'active crystals', 'flying crystals' or 'living crystals'. The activity due to self-propulsion induces properties that differ from passive crystalline clusters. For instance, it can amend the critical density and temperature at which crystallization takes place and may induce translational and rotational motion.

Recently it has been found that the active PFC model not only allows for periodic states but also for many types of resting and traveling localized states (Ophaus *et al.*, 2018). There, a detailed analysis of the underlying bifurcation structure in one spatial dimension is provided, with a particular emphasis on the onset of motion. Further details of the bifurcation structure and an investigation of the scattering behavior of traveling localized states are presented by Ophaus *et al.* (2020). First results on localized states in two dimensions are discussed by Ophaus *et al.* (2021).

In the present contribution we focus on the one-dimensional (1D) case and present an overview and comparison of the behavior of localized states in PFC systems. In particular, section 2 reviews and extends results for the classic passive PFC model, while section 3 provides an overview of the active PFC model. Then, in section 4, we present the first results for localized states in a passive binary PFC system representing a symmetric mixture of colloidal particles followed by a study of such a system with active coupling. The subsequent section 5 considers an active binary PFC system modeling a mixture of passive and active colloids. In all cases we discuss the structure of the model, sketch the linear stability results for uniform states and present typical bifurcation diagrams for steady (and traveling) localized states. All the bifurcation structures discussed below were computed employing numerical continuation techniques (Engelnkemper *et al.*, 2019; Krauskopf *et al.*, 2007) provided by the packages auto07p (Doedel *et al.*, 1991) and pde2path (Uecker *et al.*, 2014). The paper concludes with section 6.

Downloaded from https://academic.oup.com/imamat/advance-article/doi/10.1093/imamat/hxab025/6318163 by University of California, Berkeley user on 12 July 2021

Note that the data and computer codes used in sections 4.2 and 5 of our work are available from a data repository (Holl *et al.*, 2021a).

2. Slanted snaking in the passive PFC model[3]

Introducing the energy (1.2) into the mass-conserving equation (1.3) results in the kinetic equation

$$\partial_t \psi = M\nabla^2\left[r\psi + (\nabla^2 + q^2)^2\psi + (\psi + \bar{\phi})^3\right], \tag{2.1}$$

where we introduced the field $\psi \equiv \phi - \bar{\phi}$ with the property $\int_V \psi \, \mathrm{d}^n\mathbf{r} = 0$. Thus $\bar{\phi}$ becomes a parameter of the equation. In the underlying $\mathscr{F}[\phi]$ the quartic term may be replaced by other types of nonlinearity, such as f_{234} (Cox, 2004; Matthews & Cox, 2000; Tegze *et al.*, 2009; Teeffelen *et al.*, 2009) without substantial change in behavior.

Here we consider Eq. (2.1) in one dimension only, with $M = 1$ and $q = 1$, i.e.

$$\partial_t \psi = \partial_x^2\left[r\psi + (\partial_x^2 + 1)^2\psi + (\psi + \bar{\phi})^3\right]. \tag{2.2}$$

For results in 2D and 3D, see Engelnkemper *et al.* (2019), Thiele *et al.* (2013) and Thiele *et al.* (2019).

This equation is invariant under the reflection $x \to -x$, i.e. it is reversible in space. Steady states ($\partial_t \psi = 0$) are solutions of the fourth-order ordinary differential equation

$$0 = r\psi + (\partial_x^2 + 1)^2\psi + (\psi + \bar{\phi})^3 - \tilde{\mu}, \tag{2.3}$$

where $\tilde{\mu}$ is an integration constant that is directly related to the chemical potential $\mu = \delta\mathcal{F}[\phi]/\delta\phi$ by $\mu = \tilde{\mu} + (1 + r)\bar{\phi}$ (cf. Thiele *et al.*, 2013).

The typical bifurcation behavior as a function of the mean density $\bar{\phi}$ at a modest effective temperature $r = -0.9$ in the range where crystallization can occur is shown in Fig. 1 using the L^2 norm $||\psi||$ as a solution measure. The uniform, i.e. liquid, state exists at all densities. It is linearly stable at large negative $\bar{\phi}$ and becomes linearly unstable at $\bar{\phi} \approx -0.55$. For a domain of size $L = 100$, a branch of periodic or crystalline states with $n = 16$ peaks emerges in a supercritical pitchfork of revolution, bifurcation A in Fig. 1. Close to onset, states on this branch are linearly stable. Branches with other peak numbers emerge nearby but are unstable and not relevant here (not shown). Moreover, the $n = 16$ periodic states lose stability almost immediately in a further pitchfork bifurcation, bifurcation B in Fig. 1, where two branches of symmetric localized states bifurcate subcritically. The presence of this bifurcation is a consequence of mass conservation (Matthews & Cox, 2000). These localized states are symmetric with respect to reflection in their midpoint where they have a maximum ($\mathrm{LS}_{\mathrm{odd}}$, black solid line) or a minimum ($\mathrm{LS}_{\mathrm{even}}$, dashed red line). Both are initially unstable and stabilize when they fold back towards larger $\bar{\phi}$ in saddle-node bifurcations. The branches then wiggle back and forth exhibiting pronounced slanted snaking until they terminate back on the $n = 16$ periodic branch at about $\bar{\phi} \approx -0.3$ in another subcritical pitchfork bifurcation. Beyond this point, the $n = 16$ periodic branch is again stable. The two branches of symmetric localized states are connected by 14 branches of steady

[3] This section reviews and expands on aspects of Thiele *et al.* (2013). Corresponding data can be found on zenodo under http://doi.org/10.5281/zenodo.3890105.

Downloaded from https://academic.oup.com/imamat/advance-article/doi/10.1093/imamat/hxab025/6318163 by University of California, Berkeley user on 12 July 2021

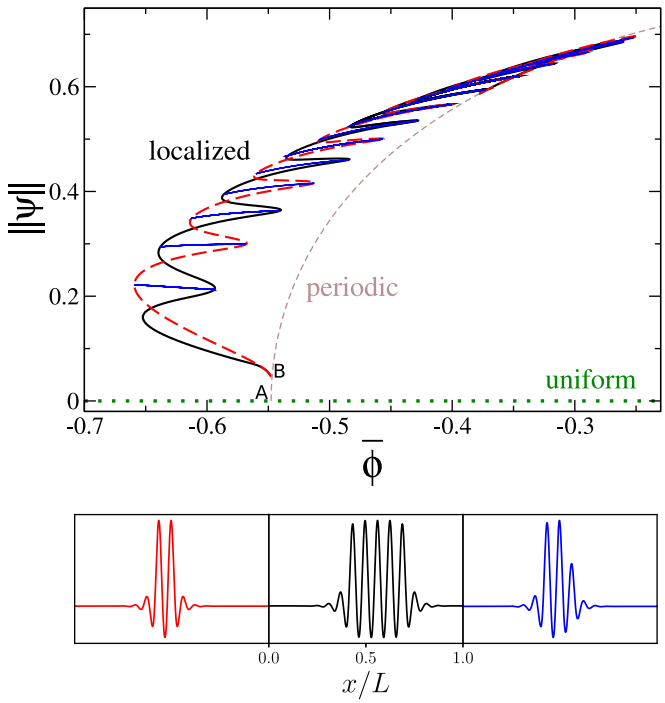

FIG. 1. Typical bifurcation diagram for steady states of the conserved SH equation (passive PFC model) in 1D [Eq. (2.2)] showing the L^2 norm $||\psi||$ as a function of the mean density $\bar{\phi}$ for fixed domain size $L = 100$ and effective temperature $r = -0.9$. The horizontal dotted green line corresponds to the uniform (liquid) state $\psi(x) = 0$, while the thin dashed brown line corresponds to periodic (crystalline) states. The intertwined solid black and dashed red lines represent slanted homoclinic snaking of symmetric steady localized states with an odd (LS_{odd}) and an even (LS_{even}) number of peaks, respectively. The solid blue lines correspond to asymmetric localized states. Together these form a slanted snakes-and-ladders structure. The primary and secondary bifurcation points are labeled A and B, respectively. The bottom panel shows color-coded examples of the three kinds of localized states. The data presented here correspond to Fig. 2(a) of Thiele *et al.* (2013).

asymmetric localized states that form the rungs of the snakes-and-ladders structure. For more details, and in particular a discussion of the changes in stability along the branches, see Thiele *et al.* (2013). We remark that with increasing domain size L the secondary pitchfork bifurcation (B) approaches the primary bifurcation (A). In the thermodynamic limit of an infinite domain localized and periodic states emerge together at the same primary bifurcation (Burke & Knobloch, 2006) (see also section 4 of Thiele *et al.*, 2019).

Next, we supplement Thiele *et al.* (2013) by discussing the bifurcation behavior when the temperature r is employed as control parameter at fixed mean density. A typical case is presented in Fig. 2 for fixed $\bar{\phi} = -0.5$. The liquid state is linearly stable at all positive and small negative r and becomes linearly unstable at $r = r_c \approx -0.75$ (in an infinite domain this threshold is given by $r_c^\infty = -3\bar{\phi}^2$). The primary bifurcation, i.e. the bifurcation A in Fig. 2, where the crystalline state emerges is again supercritical followed by a subcritical bifurcation, i.e. bifurcation B in Fig. 2, where, as above, two branches of symmetric localized states emerge. These are again connected by branches of asymmetric localized states. In contrast to Fig. 1, here the LS_{odd} and LS_{even} branches no longer terminate on the branch of periodic states but continue towards lower r although snaking stops after a finite number

Downloaded from https://academic.oup.com/imamat/advance-article/doi/10.1093/imamat/hxab025/6318163 by University of California, Berkeley user on 12 July 2021

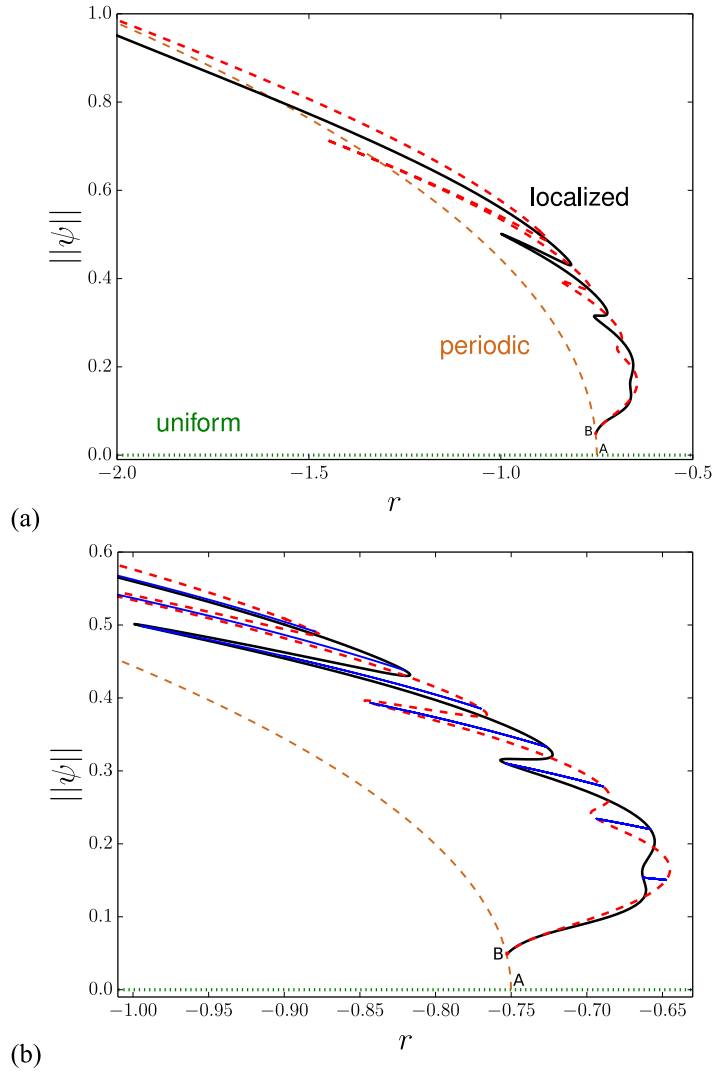

FIG. 2. Bifurcation diagram for the passive PFC model [Eq. (2.2)] using the effective temperature r as the control parameter for fixed $\bar{\phi} = -0.5$. Panel (a) shows the homogeneous, periodic and symmetric localized states. The magnification in panel (b) includes in addition the asymmetric localized states (blue rungs). The remaining parameters and line styles are as in Fig. 1. The primary and secondary bifurcation points are labeled A and B, respectively.

of saddle-node bifurcations, i.e. the localized patterned patch never fills up the entire domain. This behavior is related to changes in the overall bifurcation structure that occur below $r \approx -1.75$. These are not described here (but see Fig. 3 below) and neither are the top-hat structures involving plateaus of nonzero ψ that are present in the nonconserved SH equation (Burke & Knobloch, 2006, 2007; Ouchi & Fujisaka, 1996). Such states occur here for large negative r at appropriate $\bar{\phi}$.

Downloaded from https://academic.oup.com/imamat/advance-article/doi/10.1093/imamat/hxab025/6318163 by University of California, Berkeley user on 12 July 2021

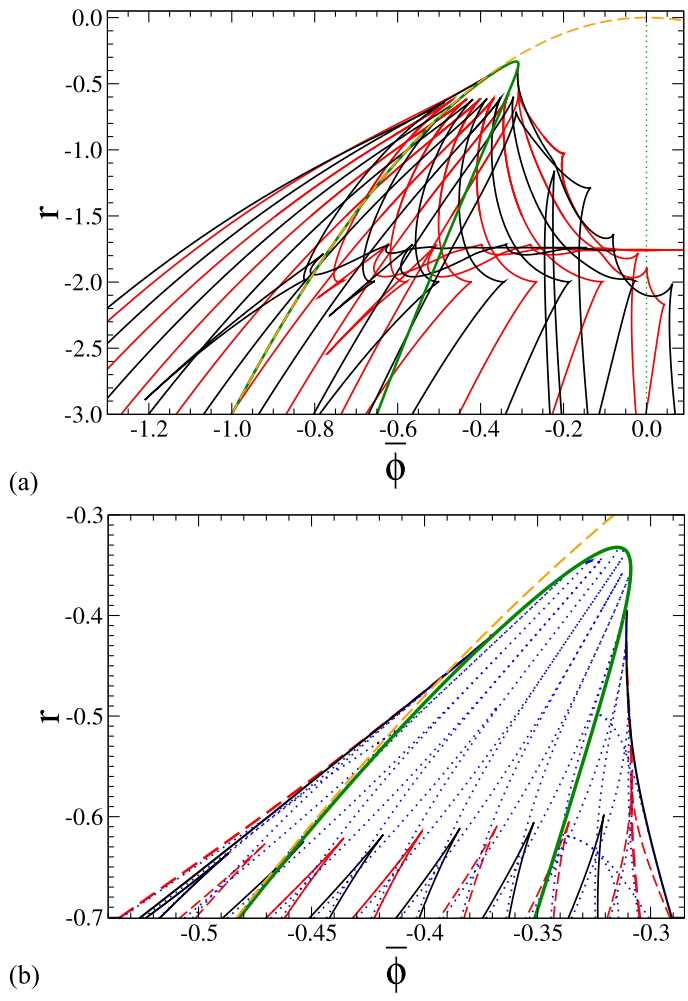

FIG. 3. (a) Loci of all saddle-node bifurcations of the branches of symmetric localized states visible in Figs. 1 and 2 in the $(\bar{\phi}, r)$ plane in the range $-3 < r < 0$. (b) Magnification of the region of (a) close to the tricritical point including the loci of all pitchfork bifurcations (dotted blue lines) where branches of asymmetric localized states emerge from branches of symmetric localized states. In both panels, the solid green line tracks the secondary bifurcations where symmetric localized states emerge from the periodic state (bifurcations B), while the dashed orange line shows the locus of the primary bifurcations A. Remaining parameters and line colors correspond to Fig. 1. The data presented in panel (a) extend Fig. 6 of Thiele *et al.* (2013) while panel (b) reproduces the data of their Fig. 7.

The snaking behavior in both Fig. 1 and Fig. 2 is summarized by tracking (using two-parameter continuation) the loci of all saddle-node bifurcations of localized states in the parameter plane spanned by the mean density and effective temperature, displayed in Fig. 3. Also shown are loci of primary (dashed orange line) and secondary (solid green line) pitchfork bifurcations where periodic and localized states emerge, i.e. bifurcations A and B, respectively. Figure 3(a) presents the results for all saddle-node bifurcations of the symmetric localized states visible in Figs. 1 and 2. Near $r = -1.75$ some of the

Downloaded from https://academic.oup.com/imamat/advance-article/doi/10.1093/imamat/hxab025/6318163 by University of California, Berkeley user on 12 July 2021

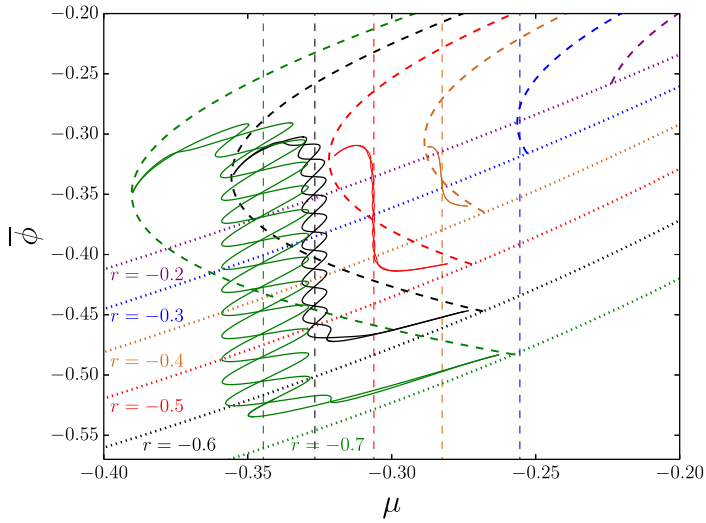

FIG. 4. Branches of liquid (dotted lines), crystalline (dashed lines) and symmetric localized (thin solid lines) steady states for the conserved SH equation (2.2) showing the mean concentration $\bar{\phi}$ as a function of the chemical potential $\mu = \tilde{\mu} + (1 + r)\bar{\phi}$ for various values of r as indicated. The vertical thin dashed lines indicate the μ-values at liquid-crystal coexistence obtained from a Maxwell construction. Remaining parameters are as in Fig. 1. The figure presents data from Figs. 2, 4 and 14 of Thiele *et al.* (2013) but in a different manner.

saddle-node bifurcations annihilate with their counterparts in the mirror snaking structure that exists for $\bar{\phi} > 0$. In this process the snaking structure breaks up into a number of isolas that bridge regions of negative and positive $\bar{\phi}$ (not shown). Figure 3(b) provides a magnification of the effective temperature range $-1 < r < -0.3$ and includes in addition the loci of all pitchfork bifurcations where branches of asymmetric localized states emerge. Both panels show the loci of primary and secondary bifurcations where the periodic states bifurcate from the uniform state and the symmetric localized states emerge from them, respectively.

From Fig. 3 we see that for increasing r the saddle-node bifurcations annihilate pairwise in hysteresis bifurcations (visible as cusps). This happens first at small $\bar{\phi}$ and successively for larger $\bar{\phi}$, alternating between the $\mathrm{LS}_{\mathrm{odd}}$ and $\mathrm{LS}_{\mathrm{even}}$ branches. Above these cusps the branches of localized states continue to wiggle, but saddle-node bifurcations are absent. Moreover, the presence of the rung states is unaffected by the pairwise annihilation of the saddle-node bifurcations and these remain and ultimately vanish one by one through collision with the secondary bifurcation B [Fig. 3(b), see also Fig. 4 of Thiele *et al.*, 2013 for accompanying bifurcation diagrams at various values of r]. Note that the secondary bifurcations B approach one another and annihilate at $r \approx -0.33$ where localized states cease to exist (Thiele *et al.*, 2013). The thermodynamic tricritical point where the first-order phase transition becomes a second-order transition is located at slightly larger $r = -9/38 \approx -0.24$ (not shown here, but see Robbins *et al.*, 2012).

Interestingly, the tricritical point does not correspond to the point where the primary bifurcation in Figs. 1 and 2 changes its character from super- to subcritical as occurs in other systems, e.g. the standard SH equation. Such a transition also exists here but occurs at a much more negative temperature, $r = -9/2$. The reason is that in systems with conserved dynamics, the natural control parameter is the mean concentration, resulting, e.g. in Fig. 1. However, thermodynamically coexisting states in a

Downloaded from https://academic.oup.com/imamat/advance-article/doi/10.1093/imamat/hxab025/6318163 by University of California, Berkeley user on 12 July 2021

two-phase region do not normally have the same mean concentration. Consequently the existence of coexisting states and the criticality of the primary bifurcation are two different questions (in contrast to a nonconserved system where the mean concentration is not an appropriate control parameter). This issue is directly related to the final point of this section, namely, the relation between the steady states and associated bifurcation diagrams of the standard (nonconserved) SH equation (1.1) and of its conserved counterpart (2.1). Note that the equation describing the steady states of the latter [Eq. (2.3)] is identical to the equation for the steady states of the SH equation (1.1) with an additional external field μ (Kozyreff & Chapman, 2006).

To determine the bifurcation diagram of Fig. 1, one solves Eq. (2.3) using $\bar{\phi}$ as a control parameter: since (2.2) conserves $\bar{\phi}$, the bifurcations in Fig. 1 correctly indicate the linear stability of states under conserved dynamics, i.e. with respect to perturbations that maintain fixed $\bar{\phi}$. However, when we change $\bar{\phi}$ along a solution branch, the chemical potential $\mu = \tilde{\mu} + (1 + r)\bar{\phi}$ has to be adapted as it corresponds to the Lagrange multiplier enforcing mass conservation. This allows us to present the same steady state branches using μ as the control parameter, as shown for a number of r-values in Fig. 4.

Remarkably, in the latter representation, the slanted snaking of Fig. 1 becomes vertically aligned snaking centered about the chemical potential value at coexistence (as obtained from a Maxwell construction). Although this alternative representation has 'straightened' the slanted snaking into vertically aligned snaking, it invalidated the diagram as a bifurcation diagram for steady states of the conserved system since it no longer reflects stability with respect to perturbations at fixed $\bar{\phi}$. Instead, with μ as the control parameter, the bifurcations in Fig. 4 indicate linear stability under nonconserved dynamics, Eq. (1.1), at fixed imposed chemical potential (or external field) μ. For such nonconserved dynamics, all perturbations are at fixed μ and so allow for a variation in $\bar{\phi}$. In this case, the transition between first- and second-order phase transitions coincides with the transition between subcritical and supercritical bifurcations because the existence of coexisting states and the criticality of the primary bifurcation are in fact the same question. For further discussion of this point, see the conclusion of Thiele *et al.* (2013) and Engelnkemper *et al.* (2019), where this issue is also discussed for nonconserved and conserved Allen–Cahn equations. The latter is also known as the Cahn–Hilliard equation.

3. Traveling localized states in an active PFC model[4]

To obtain a simple dynamical continuum model for the crystallization processes of active colloids, the PFC equation (2.1) is coupled with the dynamics of a polarization field $\mathbf{P}$ that indicates the local strength and direction of polar order and the related active drive. The polarization is a vectorial order parameter with nonconserved dynamics. The resulting coupled system is the active PFC model (Menzel & Löwen, 2013)

$$\begin{aligned} \partial_t \psi &= \nabla^2 \frac{\delta \mathscr{F}}{\delta \psi} - \alpha \nabla \cdot \mathbf{P}, \\ \partial_t \mathbf{P} &= \nabla^2 \frac{\delta \mathscr{F}}{\delta \mathbf{P}} - D_{\mathrm{r}} \frac{\delta \mathscr{F}}{\delta \mathbf{P}} - \alpha \nabla \psi, \end{aligned} \tag{3.1}$$

[4] This section reviews aspects of Ophaus *et al.* (2018) and Ophaus *et al.* (2020). Corresponding data can be found on zenodo under http://doi.org/10.5281/zenodo.4322991.

Downloaded from https://academic.oup.com/imamat/advance-article/doi/10.1093/imamat/hxab025/6318163 by University of California, Berkeley user on 12 July 2021

where α is the coupling strength, also called the activity parameter or velocity of self-propulsion. The polarization is subject to translational and rotational diffusion with D_r as the rotational diffusion constant. The energy functional

$$\mathscr{F}[\psi, \mathbf{P}] = \mathscr{F}_\mathrm{sh}[\psi] + \mathscr{F}_\mathbf{P}[\mathbf{P}] \tag{3.2}$$

is the sum of the standard PFC functional (1.2) and an orientational part,

$$\mathscr{F}_\mathbf{P}[\mathbf{P}] = \int \mathrm{d}^n\mathbf{r} \left(\tfrac{1}{2} c_1 |\mathbf{P}|^2 + \tfrac{1}{4} c_2 |\mathbf{P}|^4 \right). \tag{3.3}$$

With no coupling between the density ψ and polarization $\mathbf{P}$, i.e. at $\alpha = 0$, the dynamics of ψ correspond to conserved gradient dynamics on $\mathscr{F}_\mathbf{sh}[\psi]$, while $\mathbf{P}$ follows mixed gradient dynamics, i.e. a combination of conserved (first term) and nonconserved (second term) gradient dynamics on $\mathscr{F}_\mathbf{P}[\mathbf{P}]$. The employed coupling of density and polarization cannot be written in gradient dynamics form and corresponds to the simplest possible nonvariational coupling that is compatible with the tensorial and conservation character of the two equations: density gradients cause polarization and polarization drives the density field (Menzel & Löwen, 2013).

Although the functional $\mathscr{F}_\mathbf{P}$ with $c_1 < 0$ and $c_2 > 0$ allows for spontaneous polarization most works consider the simpler case $c_1 > 0$ and $c_2 = 0$ (Chervanyov *et al.*, 2016; Menzel & Löwen, 2013; Menzel *et al.*, 2014; Ophaus *et al.*, 2018). Then, spontaneous polarization is absent and polarization is solely generated in response to density gradients while the variational part of its dynamics, i.e. diffusion, is always dissipative. We focus here on the latter case. Introducing the functional derivatives of (1.2) and (3.3) into the governing equations (3.1) this case is described by the nondimensional evolution equations

$$\partial_t \psi = \nabla^2 \left\{ \left[r + \left(1 + \nabla^2\right)^2 \right] \psi + \left(\bar{\phi} + \psi\right)^3 \right\} - \alpha \nabla \cdot \mathbf{P}, \tag{3.4}$$

$$\partial_t \mathbf{P} = c_1 \nabla^2 \mathbf{P} - D_\mathrm{r} c_1 \mathbf{P} - \alpha \nabla \psi. \tag{3.5}$$

In 1D the polarization $\mathbf{P}(\mathbf{r})$ becomes a scalar $P(x)$ that represents the strength and direction of the polarization at location x, while ∇ and ∇^2 are replaced by ∂_x and ∂_x^2, respectively. The behavior of solutions of Eqs. (3.4) and (3.5) has been studied by Chervanyov *et al.* (2016); Menzel & Löwen (2013); Menzel *et al.* (2014); Ophaus *et al.* (2018, 2020) and Ophaus *et al.* (2021) by means of linear stability analysis of the uniform state, direct time simulations in 1D and 2D and by numerical bifurcation analysis tracking various nonlinear states and their linear stability.

Equation (3.4), like Eq. (2.1), conserves ψ and hence $\int_V \psi \, \mathrm{d}^n\mathbf{r} = 0$. This in turns implies that in the long-time limit $\int_V \mathbf{P} \, \mathrm{d}^n\mathbf{r} = 0$. However, in contrast to the passive PFC model reviewed in section 2 that exhibits small-scale stationary linear instabilities and steady nonlinear states, the nonvariational character of the active model allows in addition for short-wave oscillatory linear instability modes of the uniform state and the presence of primary Hopf bifurcations, as well as for drift bifurcations whereby traveling nonlinear states emerge from steady ones. As for the passive PFC model, in the active PFC model, there exist domain-filling periodic states (Menzel & Löwen, 2013) as well as localized states (Ophaus *et al.*, 2018) where finite patches of resting or traveling crystalline states coexist with a uniform background. However, as the model is nonvariational, the presence of these states cannot be related to a Maxwell construction in the thermodynamic limit as done for the passive case by Thiele *et al.* (2019).

Downloaded from https://academic.oup.com/imamat/advance-article/doi/10.1093/imamat/hxab025/6318163 by University of California, Berkeley user on 12 July 2021

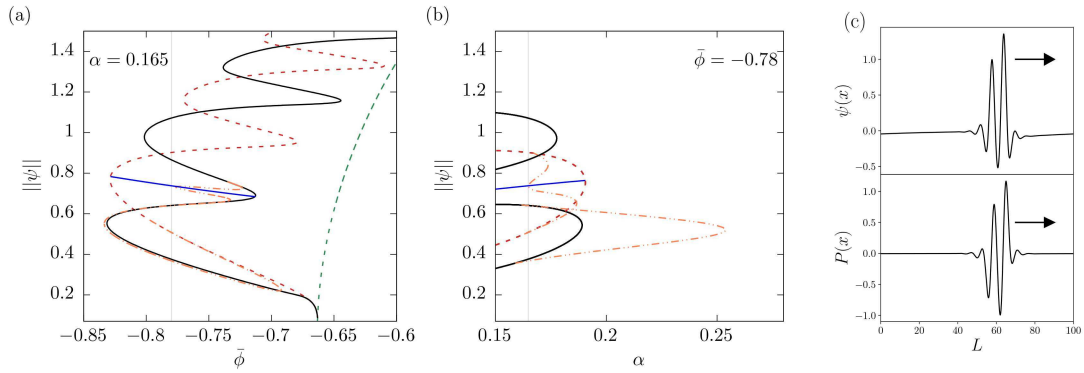

FIG. 5. Typical bifurcation diagrams for the one-species active PFC model [Eqs. (3.4) and (3.5)] in 1D focusing on branches of steady and traveling localized states using (a) the mean density $\bar{\phi}$ at fixed $\alpha = 0.165$ and (b) the activity parameter α at fixed $\bar{\phi} = -0.78$ as control parameters. Steady symmetric localized states with an even and an odd number of peaks are shown as dashed red and solid black lines, respectively. Also included are steady asymmetric localized states (blue lines), traveling localized states (dot-dashed lines), and periodic steady states with $n = 16$ peaks (green dashed line). For clarity, only branches of asymmetric and traveling localized states connecting stationary one- and two-peak states are shown. Vertical gray lines indicate the value of the parameter fixed in the complementary panel. Panel (c) shows a sample traveling localized state at $\bar{\phi} = -0.8$, $\alpha = 0.165$. The remaining parameters are $r = -1.5$, $c_1 = 0.1$, $c_2 = 0$ and $D_r = 0.5$. The domain size is $L = 100$. The data presented in panels (a) and (b) extend Figs. 5 and 9(c) of Ophaus *et al.* (2018), respectively. Also see their Figs. 11 and 12.

Figures 5(a) and (b) present examples of typical bifurcation behavior of steady and traveling localized states in 1D employing the mean density $\bar{\phi}$ and the activity parameter α as main control parameters, respectively. In panel (a) one sees that steady localized states again exhibit slanted homoclinic snaking qualitatively similar to the passive case shown in Fig. 1. Only the first few wiggles are shown in order to reveal the finer details. Increasing $\bar{\phi}$, the uniform state becomes linearly unstable at $\bar{\phi} \approx -0.66$ where the $n = 16$ periodic state bifurcates supercritically (green dashed line). The latter becomes unstable at small amplitude giving rise to two branches (black and red dashed) of steady symmetric localized states that emerge in a subcritical secondary pitchfork bifurcation just as in the passive case. The resulting branches of symmetric steady localized states with even and odd number of peaks are again connected by branches of asymmetric steady localized states (blue lines). Their existence as steady states is related to the linear coupling in Eqs. (3.4) and (3.5) and the 'accidental' global conservation of P mentioned above. Increasing c_2 from zero in (3.3) or introducing a nonlinear coupling causes all rung states to drift, a behavior that will be discussed further elsewhere.

Qualitatively new in the active PFC model, as compared to in the passive PFC model, are the branches of traveling localized states (dot-dashed orange lines). These emerge from the branches of resting symmetric localized states in a drift-pitchfork bifurcation and may connect to branches of steady asymmetric localized states via drift-transcritical bifurcations. The resulting states drift with a constant velocity that depends on the control parameters. A detailed discussion of the onset of motion (including an analytical condition) and typical profiles of resting and traveling states can be found in Ophaus *et al.* (2018). Figure 5(c) shows one example of such a traveling localized state and reveals that such states are quite similar to their resting counterparts. The main difference is a small phase shift between the fields ψ and P associated with the motion that increases with increasing activity (and drift speed). Note that Fig. 5(a) shows the case of relatively low, $\alpha = 0.165 < \alpha_c$, close to but below the critical activity value

Downloaded from https://academic.oup.com/imamat/advance-article/doi/10.1093/imamat/hxab025/6318163 by University of California, Berkeley user on 12 July 2021

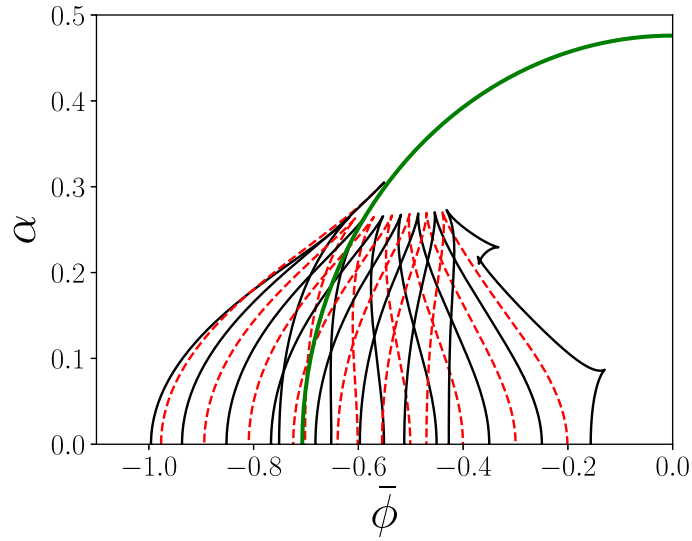

FIG. 6. Loci of saddle-node bifurcations on the branches of resting symmetric localized states with even (dashed red lines) and odd (solid black lines) numbers of peaks in the $(\bar{\phi}, \alpha)$ plane. The locus of the primary bifurcation to periodic states is shown as a thick green line. The remaining parameters are as in Fig. 5. The figure presents data from Fig. 7(a) of Ophaus *et al.* (2020) but in a different manner.

α_c where the primary bifurcation becomes oscillatory. Slanted homoclinic snaking of traveling states at $\alpha > \alpha_c$ is also possible.

Figure 5(b) shows that an increase of the activity parameter α at fixed $\bar{\phi}$ may result in a transition from steady to traveling localized states. The α values for the onset of motion for the various states are very similar, but not identical. An interesting feature is the 'nose' of traveling states that reaches far beyond the α-range that allows for steady localized states. The location of the terminating saddle-node bifurcation depends strongly on $\bar{\phi}$ and may even diverge to $\alpha \to \infty$ (cf. Figs. 8 and 9 in Ophaus *et al.*, 2018). The existence regions of the various localized states and the scattering behavior of traveling localized states are investigated by Ophaus *et al.* (2020). There the occurrence of more complex localized states corresponding, e.g. to localized standing waves and traveling modulated waves, is also discussed.

We show, finally, how the location of the saddle-node bifurcations in Fig. 5 depends on the complementary control parameter. In particular, Fig. 6 tracks their location in the $(\bar{\phi}, \alpha)$ plane. It is remarkable that the overall structure is very similar to Fig. 3 with the activity in Fig. 6 taking the role of the effective temperature in Fig. 3. This observation merits further investigation.

4. Two coupled PFC models

A relatively simple continuum model for the crystallization dynamics of a mixture of two species of colloidal particles is obtained by coupling two PFC equations. To study the behavior of a thermodynamic system the coupling is taken to be variational, while in the study of active colloids a nonvariational coupling may be considered. Here, we focus on a linear coupling containing variational and nonvariational (or nonreciprocal) contributions of strength c and α, respectively. The resulting

Downloaded from https://academic.oup.com/imamat/advance-article/doi/10.1093/imamat/hxab025/6318163 by University of California, Berkeley user on 12 July 2021

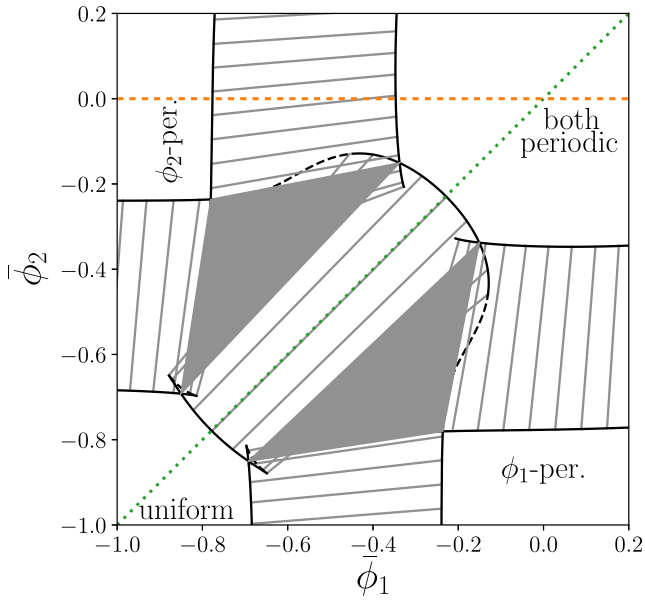

FIG. 7. Phase diagram for the two-species passive PFC model [Eq. (4.1)] in 1D with $\alpha = 0$ in the plane spanned by the mean densities $\bar{\phi}_1$ and $\bar{\phi}_2$. The hatched [gray shaded] areas represent regions of coexistence of two [three] phases, and the gray tie lines connect particular coexisting states on pairs of binodal lines. The green dotted and orange dashed straight lines correspond to the paths taken in the bifurcation diagrams of Figs 8 and 9, respectively. The remaining parameters are $r = -0.9$ and $c = -0.2$. The figure presents data from Figs. 8(a) and 9 of Holl *et al.* (2021b) but in a different manner.

equations

$$\begin{aligned}\partial_t\psi_1 &= \partial_x^2[r\psi_1 + (\partial_x^2 + q_1^2)^2\psi_1 + (\psi_1 + \bar{\phi}_1)^3 + (c+\alpha)\psi_2],\\ \partial_t\psi_2 &= \partial_x^2[r\psi_2 + (\partial_x^2 + q_2^2)^2\psi_2 + (\psi_2 + \bar{\phi}_2)^3 + (c-\alpha)\psi_1]\end{aligned} \tag{4.1}$$

are parity symmetric, i.e. invariant w.r.t. a reflection in x, and also have the inversion symmetry $\bar{\phi}_j + \psi_j \to -(\bar{\phi}_j + \psi_j)$. The dynamics conserves both mean densities $\bar{\phi}_j$, i.e. the ψ_j again represent deviations from the mean with $\int_V \psi_j \,\mathrm{d}x = 0$. Without nonreciprocal coupling, i.e. for $\alpha = 0$, the model reduces to that presented by Elder *et al.* (2002) and represents conserved gradient dynamics on the energy functional

$$\mathscr{F}[\phi_1, \phi_2] = \mathscr{F}_{\mathrm{sh}}[\phi_1] + \mathscr{F}_{\mathrm{sh}}[\phi_2] + \mathscr{F}_{\mathrm{int}}[\phi_1, \phi_2] \tag{4.2}$$

with $\mathscr{F}_{\mathrm{int}}[\phi_1, \phi_2] = \int c\phi_1\phi_2 \,\mathrm{d}x$. In principle, the two species of colloidal particles do not need to have the same typical length scale q_j nor the same coefficients of the gradient energy or local energy terms. However, here we keep things simple and consider only the case $q_1 = q_2 = 1$. We also use the same coefficients in all the other terms.

In section 4.1 we focus on the fully variational case and subsequently explore two ways of making the model active. In particular, section 4.2 considers Eqs. (4.1) with $\alpha \neq 0$ while section 5 uses $\alpha = 0$ but couples one of the densities to a polarization in a similar fashion as in section 3.

Downloaded from https://academic.oup.com/imamat/advance-article/doi/10.1093/imamat/hxab025/6318163 by University of California, Berkeley user on 12 July 2021

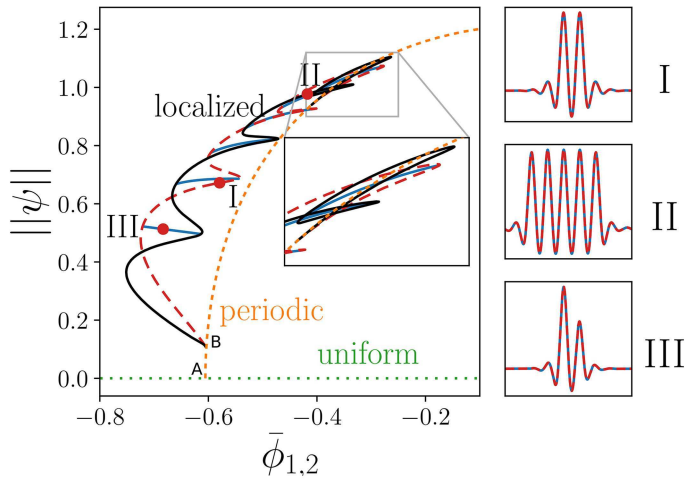

FIG. 8. Typical bifurcation diagram using the mean density $\bar{\phi} = \bar{\phi}_1 = \bar{\phi}_2$ as a control parameter, crossing from the uniform liquid state into the crystalline alloy existence region along the diagonal dotted green line in Fig. 7. Steady symmetric localized states with even and odd numbers of peaks are shown as dashed red and solid black lines, respectively. Also included are steady asymmetric localized states (blue lines), the trivial uniform (liquid) state (dotted green line) and periodic steady states with $n = 8$ peaks (dashed orange line). The small panels I to III show a selection of concentration profiles on the various branches of localized states at locations indicated by the filled red circles in the main panel. As in Fig. 1 the primary and secondary bifurcation points are labeled 'A' and 'B', respectively. The inset magnifies the region where the localized states reconnect to the periodic branch. The remaining parameters are as in Fig. 7.

From here on, the domain size is $L = 16\pi$, corresponding to eight peaks at the onset of instability. The smaller domain results in bifurcation diagrams that are less crowded and easier to read. We expect qualitatively similar behavior for larger domains.

4.1 *Variational coupling*[5]

We set $\alpha = 0$ in Eq. (4.1) to retain the variational character of the coupled PFC equations. In this case only resting states occur.

The passive system describes the crystallization behavior of a mixture of two species of colloid allowing for various liquid and crystalline phases. Holl *et al.* (2021b) employ continuation techniques to study in detail the thermodynamic phase behavior of the model in one and two dimensions. Figure 7 presents one quadrant of a typical phase diagram in the $(\bar{\phi}_1, \bar{\phi}_2)$ plane in 1D. The phase plane features four distinct phases: a low-density uniform (well-mixed liquid) phase, and three different periodic (crystal) phases. The latter are a ϕ_1-crystal in which the amplitude of the ϕ_1 modulation is much larger than that in ϕ_2, the corresponding ϕ_2-crystal, and a crystalline 'alloy' phase where the amplitudes of the periodic modulation in both fields are similar.

The boundaries between the various phases in Fig. 7 are formed by two-phase coexistence regions indicated by pairs of binodal lines and three-phase coexistence regions. Particular coexisting states on the binodal lines are connected by straight tie lines. The continuation of binodal lines beyond the corners

[5] This section reviews aspects of Holl *et al.* (2021b) and adds information on localized states. Corresponding data and computer codes can be found on zenodo under http://doi.org/10.5281/zenodo.4269554.

Downloaded from https://academic.oup.com/imamat/advance-article/doi/10.1093/imamat/hxab025/6318163 by University of California, Berkeley user on 12 July 2021

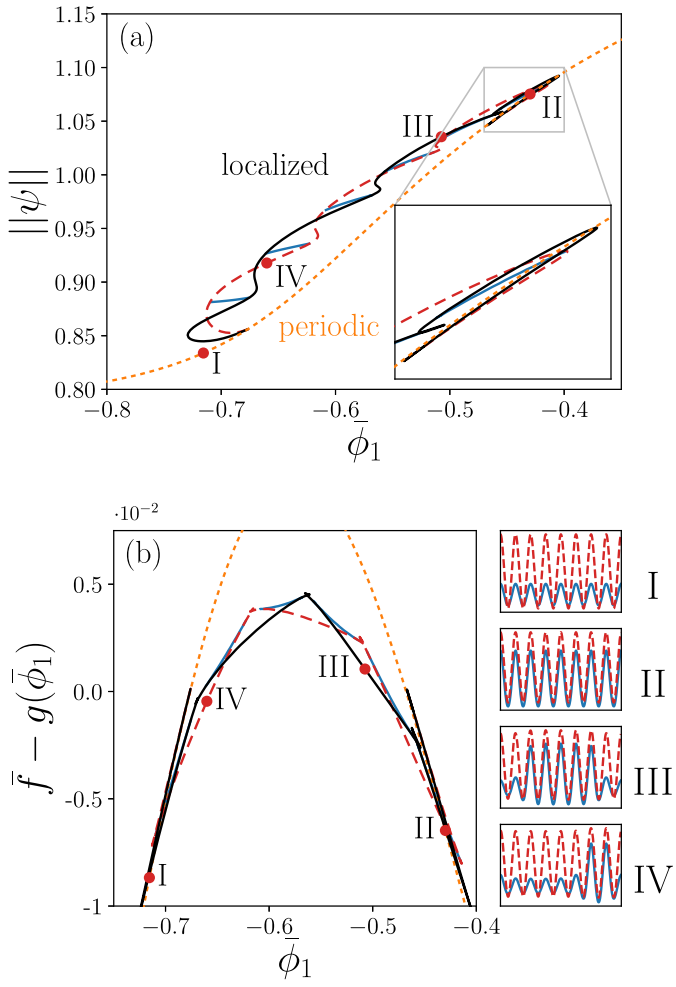

FIG. 9. (a) Typical bifurcation diagrams using the mean density $\bar{\phi}_1$ as the control parameter at fixed $\bar{\phi}_2 = 0$, crossing the coexistence region of the ϕ_2-crystal and the crystalline alloy along the dashed horizontal line in Fig. 7. Line styles are as in Fig. 8 while the remaining parameters are as in Fig. 7. The inset magnifies the region where the localized states reconnect to the periodic states. (b) Corresponding mean free energy densities $\bar{f}$, showing that localized states are the lowest energy states in the coexistence region. A linear function $g(\bar{\phi}_1) = a\bar{\phi}_1 + b$, corresponding to a straight line connecting the bifurcation points where the localized states emerge $[(\bar{\phi}_1^A, \bar{f}^A) \approx (-0.6762, -0.1596)]$ and terminate $[(\bar{\phi}_1^B, \bar{f}^B) \approx (-0.6762, -0.1596)]$, has been subtracted to allow one to visually differentiate the various lines. The small panels I to IV give a selection of the concentration profiles on the various branches as indicated by the filled red circles in (a) and (b).

of the shaded triangles corresponds to metastable (solid lines) and unstable (dashed lines) coexistence. Note that the three-phase coexistence region corresponds to a triple point. For further details, see Holl *et al.* (2021b). The straight dotted and dashed lines show the parameter paths we take to determine bifurcation diagrams related to liquid–crystal and crystal–crystal phase transitions, presented in Figs. 8 and 9, respectively.

Downloaded from https://academic.oup.com/imamat/advance-article/doi/10.1093/imamat/hxab025/6318163 by University of California, Berkeley user on 12 July 2021

Downloaded from https://academic.oup.com/imamat/advance-article/doi/10.1093/imamat/hxab025/6318163 by University of California, Berkeley user on 12 July 2021

Figure 8 follows the path along the diagonal using $\bar{\phi} = \bar{\phi}_1 = \bar{\phi}_2$ as the control parameter, passing from the liquid phase into the crystalline alloy phase. As there is complete symmetry between the two fields, the bifurcation diagram is rather similar to Fig. 1. The uniform state becomes linearly unstable at $\bar{\phi} \approx -0.61$ where the branch of periodic states with $n = 8$ peaks emerges in a supercritical pitchfork of revolution (A). These states are initially linearly stable but lose stability in a secondary pitchfork bifurcation (B) where branches of odd ($\mathrm{LS}_{\mathrm{odd}}$) and even ($\mathrm{LS}_{\mathrm{even}}$) symmetric localized states bifurcate subcritically as in section 2. Six rungs of steady asymmetric localized states (blue curves) connect the two branches of symmetric states. When the domain is filled, the branches of localized states terminate back on the $n = 8$ periodic state. The slanted snaking structure is less dense than in Fig. 1 since the domain is smaller.

In contrast, Fig. 9(a) follows a path using $\bar{\phi}_1$ as the control parameter at fixed $\bar{\phi}_2 = 0$, passing the phase boundary from the ϕ_2-crystal into the crystalline alloy. In the transition region localized states in ϕ_1 exist on a background of a domain-filling periodic state in ϕ_2. Starting at small values of $\bar{\phi}_1$ states on the branch of periodic states have a large amplitude in ϕ_2 and a small amplitude in ϕ_1. When $\bar{\phi}_1$ increases, the periodic state becomes unstable at $\bar{\phi}_1 \approx -0.68$ where two branches of localized states emerge at a subcritical pitchfork bifurcation. The $\mathrm{LS}_{\mathrm{odd}}$ state is again stabilized when it folds back in a saddle-node bifurcation, while the $\mathrm{LS}_{\mathrm{even}}$ branch is stabilized after a saddle-node and a subsequent pitchfork bifurcation, where the first rung branch of steady asymmetric localized states emerges. In the same manner as before, the localized states form a strongly slanted snakes-and-ladders structure along which more and more density peaks are added at the edges of the localized states with a strong focus on the ϕ_1 field. When peaks of both fields fill the domain the snaking branches terminate on the periodic branch in another subcritical bifurcation. There, the periodic branch regains its linear stability and features crystalline alloy states, with similar (large) modulation amplitudes in both fields.

Interestingly, it is not possible to spot the ϕ_2-crystal to crystalline alloy first-order phase transition by examining only the branch of periodic states as it is smooth and shows no special features in the representation of Fig. 9(a). Indeed, it is the existence of localized states as global energy minima [see Fig. 9(b)] that indicates the phase transition. The phase transition can most easily be spotted when plotting the mean grand potential over the appropriate chemical potential, as it is then related to a swallow tail structure (not shown here, but see Holl *et al.*, 2021b).

To summarize, the two bifurcation diagrams presented in Figs 8 and 9 consider the same finite-size system but along two paths across regions where different first-order phase transitions occur. In Fig. 8 the background state is of a different symmetry than the pattern forming the localized state while in Fig. 9 background and localized state share the same symmetry. This difference matters when approaching the thermodynamic limit (not shown): in the case of Fig. 8 the secondary bifurcation where the branches of localized states emerge approaches the primary bifurcation as the domain size increases, much as in the one-field PFC model analyzed in section 4 of Thiele *et al.* (2019). This does not occur for the case in Fig. 9. There, no primary bifurcation is nearby and the secondary bifurcations approach some unspecific limiting point. Note that, as the tie lines in Fig. 7 are not lines of fixed $\bar{\phi}_1$ or $\bar{\phi}_2$, the approach to the thermodynamic limit for a diagram like Fig. 9 (at fixed $\bar{\phi}_2 = 0$) does not correspond to approaching a Maxwell construction. We do not consider here how the loci of saddle-node bifurcations change with the coupling strength c or the effective temperature r but expect the behavior to be similar to Fig. 1.

4.2 *Nonvariational coupling*

Next, we briefly consider the case of nonvariational coupling, i.e. Eq. (4.1) with $\alpha \neq 0$. To directly obtain an overview of the influence of the nonvariational coupling strength α on the snaking behavior,

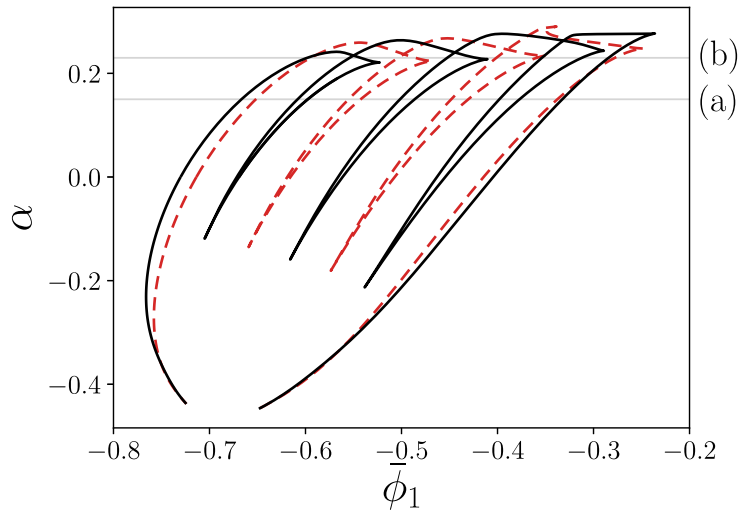

FIG. 10. Characterization of localized states in the nonvariational two-field PFC model, Eq. (4.1) with $\alpha \neq 0$. Shown are the loci of all saddle-node bifurcations that are present at $\alpha = 0$ on the branches of steady symmetric localized states in the $(\bar{\phi}_1, \alpha)$ plane. The dashed red and solid black lines indicate states with even and odd peak numbers, respectively. The thin gray horizontal lines labeled (a) and (b) indicate the paths taken in the bifurcation diagrams in Fig. 11(a) and (b), respectively. The remaining parameters are as in Fig. 9.

we consider how the loci of all saddle-node bifurcations in Fig. 9 change with α. The result is shown in Fig. 10. We note that with increasing $|\alpha|$, saddle-node bifurcations approach each other in the $(\bar{\phi}_1, \alpha)$ plane and eventually annihilate with one another. However, this occurs in a different manner for positive and negative α. For decreasing $\alpha < 0$ the behavior is quite similar to what we see in the passive one-field PFC for increasing temperature r [cf. Fig. 3(b)] or in the active one-field PFC for increasing activity [cf. Fig. 6]. Namely, the saddle-node bifurcations disappear pairwise in cusp-like structures within the range $\alpha \approx -0.12 \cdots - 0.22$. As a result, the cusps corresponding to folds of localized states that fill larger portions of the domain disappear last. The outer saddle-node bifurcations disappear when the secondary bifurcations become supercritical, at about $\alpha \approx -0.44$. As in the models considered previously, a 'wiggling' slanted structure without saddle-node bifurcations persists to lower α and corresponds to localized states that continuously increase in size along the branch. These states ultimately disappear at yet smaller α, but the periodic states continue to exist.

In contrast, for increasing $\alpha > 0$, the pairs of saddle-node bifurcations that annihilate for negative α now drift apart (see Fig. 10). Shortly above $\alpha = 0.2$ the right folds annihilate with the next-nearest left folds on their left, created at a lower value of $\bar{\phi}_1$, while the nearest left folds annihilate with the next-nearest right folds on their right, created at a higher value of $\bar{\phi}_1$. This complex structure implies that a major reorganization of the bifurcation diagram at constant α must occur. This is shown in Fig. 11. Panel (a) presents a cut through Fig. 10 at $\alpha = 0.15$ below the region where the cusps occur. The branches of in-phase modulation of the two densities (that is stable at large and small $\bar{\phi}_1$) and of anti-phase modulation are shown as a function of $\bar{\phi}_1$ with one sample profile each. The behavior is very similar to the passive case in Fig. 9. In particular, the asymmetric rung states are again steady as in the active PFC model in section 3, a fact that is again related to the linear coupling in Eqs. (4.1) as explained elsewhere.

Downloaded from https://academic.oup.com/imamat/advance-article/doi/10.1093/imamat/hxab025/6318163 by University of California, Berkeley user on 12 July 2021

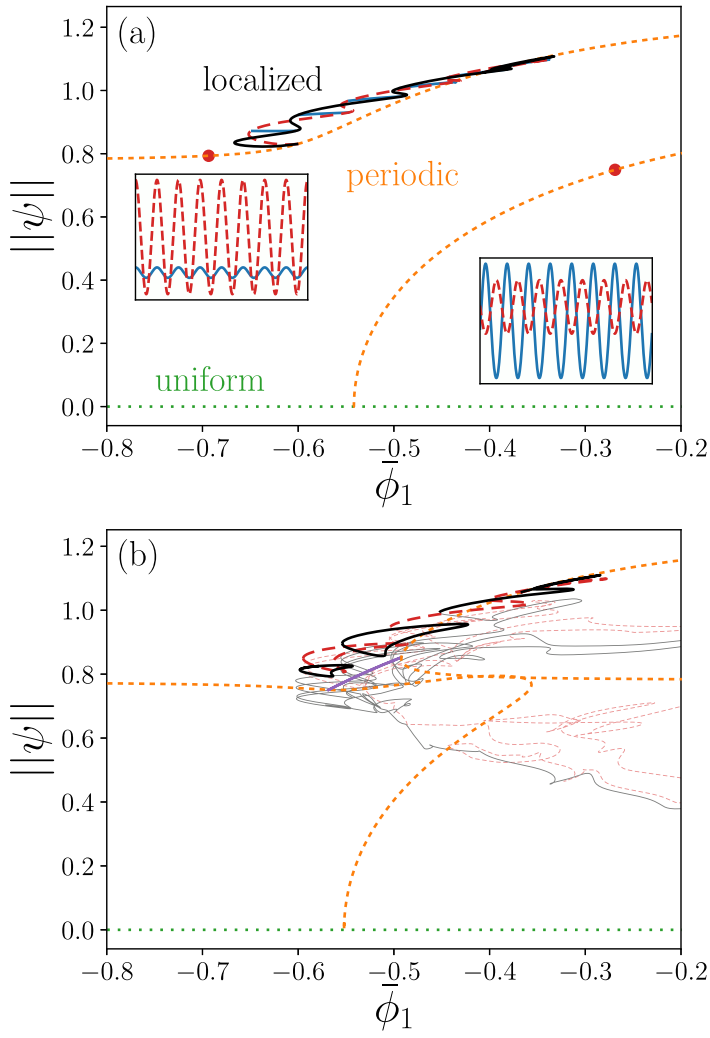

FIG. 11. Typical bifurcation diagrams for the nonvariationally coupled two-field PFC model. The mean density $\bar{\phi}_1$ is used as a control parameter at fixed $\bar{\phi}_2 = 0$ for (a) $\alpha = 0.15$ and (b) $\alpha = 0.23$, i.e. corresponding to cuts through Fig. 10 along the horizontal gray lines. Line styles are as in Fig. 8 while the remaining parameters are as in Fig. 10. (a) Slanted snaking. Filled red dots indicate the location of the sample profiles in the insets. (b) Isola generation. Thin gray solid [pink dashed] lines represent additional branches of mostly unstable $\mathrm{LS}_{\mathrm{odd}}$ [$\mathrm{LS}_{\mathrm{even}}$] states beyond the last saddle-node bifurcation known from Fig. 10. The thick purple line corresponds to traveling periodic states.

Figure 11(b) follows a cut through Fig. 10 at $\alpha = 0.23$, i.e. after the first three right-pointing cusps have already occurred. We see that the bifurcation behavior is tremendously more involved than in Fig. 11(a). When the variational and nonvariational coupling parameters have the same absolute strength, i.e. $\alpha = -c$, Eqs. (4.1) partially decouple and the two branches of periodic states meet in a codimension-2 transcritical bifurcation and reconnect in the opposite sense, i.e. at larger α the branches with anti-phase modulation continue towards smaller $\bar{\phi}_1$, while the branch of in-phase modulation

Downloaded from https://academic.oup.com/imamat/advance-article/doi/10.1093/imamat/hxab025/6318163 by University of California, Berkeley user on 12 July 2021

forms an isola at small $|\bar{\phi}_1|$. The branch of anti-phase modulations is stable at low $\bar{\phi}_1$ until it is destabilized at $\bar{\phi}_1 \approx -0.58$. A second bifurcation on that branch, at $\bar{\phi}_1 \approx -0.57$, generates a branch of traveling periodic states. The isola of periodic in-phase modulation is composed of stable solutions for $|\bar{\phi}_1| < 0.37$ where both fields show a large amplitude modulation, i.e. a large L^2 norm. At the bifurcation at $\bar{\phi}_1 \approx -0.37$, the branch of in-phase modulation is destabilized and, as in Figs. 11(a) and 9, two branches of localized states emerge. At $\alpha \approx 0.23$ these two branches undergo the last four saddle-node bifurcations that were also present at $\alpha = 0$, before undergoing a complex series of bifurcations that we do not study in detail, as the states on these branches are mostly unstable and each of the branches exhibits more than 50 saddle-node bifurcations, similarly many Hopf bifurcations and more than 100 pitchfork bifurcations. In Fig. 11(b) the branches of localized states beyond these four saddle-node bifurcations are shown in light gray [pink]. As can be seen in Fig. 10 the remaining saddle-node bifurcations present at $\alpha = 0$ are still present at $\alpha = 0.23$, even though the corresponding parts of the snaking branches are no longer connected to the periodic branches. At $\alpha = 0.23$, two right-pointing cusps involving states with odd peak numbers and one involving states with an even number of peaks have already occurred. Correspondingly, in Fig. 11(b), we find three isolas of localized states, one with an even number of peaks and two with an odd number of peaks. This indicates that at each of the right-pointing cusps in Fig. 10 one of the isolas buds off from the snaking branch. Even though the snaking branches are broken up, we can still recover the main features of snaking behavior.

It is important to note that while the bifurcation diagram in Fig. 11(b) looks very complicated, at every value of $\bar{\phi}_1$ there still exists at least one simple linearly stable steady state, i.e. a state that is known from the passive case $\alpha = 0$. In addition, there are also branches of traveling localized states at the parameter values of Fig. 11(b). For clarity, these are omitted from the bifurcation diagram.

5. Coupling active and passive PFC models

Finally, we look at a mixture of passive and active colloids by coupling a passive PFC model as in section 2 and an active PFC model as in section 3. In 1D the model is

$$\begin{aligned}
\partial_t \psi_1 &= \partial_x^2[r\psi_1 + (\partial_x^2 + 1)^2\psi_1 + (\psi_1 + \bar{\phi}_1)^3 + c\psi_2] - \alpha\partial_x P,\\
\partial_t \psi_2 &= \partial_x^2[r\psi_2 + (\partial_x^2 + 1)^2\psi_2 + (\psi_2 + \bar{\phi}_2)^3 + c\psi_1],\\
\partial_t P &= c_1\partial_x^2 P - D_r c_1 P - \alpha\partial_x\psi_1,
\end{aligned} \tag{5.1}$$

i.e. we combine a variational linear coupling (via the coupling strength c) between two densities ψ_1 and ψ_2 as in section 4.1 with a coupling of the active density ψ_1 to the polarization field P (via the coupling strength α) in a similar manner as in section 3. The density ψ_2 represents a passive field and does not contribute to the polarization.

As before, we obtain an initial overview of the snaking behavior with changing α by tracking the loci of the saddle-node bifurcations at constant $\bar{\phi}_2 = -2$ in the $(\bar{\phi}_1, \alpha)$ plane (see Fig. 12) and along the diagonal $\bar{\phi} = \bar{\phi}_1 = \bar{\phi}_2$ in the $(\bar{\phi}, \alpha)$ plane (see Fig. 13). As in section 3 we choose $r = -1.5$.

We focus first on the case in Fig. 12. At the low mean density of $\bar{\phi}_2 = -2$ the field ψ_2 is suppressed and has no major influence on the behavior of the system. We therefore expect to find behavior similar to the active PFC model in section 3. Indeed, Fig. 12 resembles Fig. 6. The saddle-node bifurcations annihilate at $\alpha \approx 0.25$ and the activity again takes the role of the effective temperature in Fig. 3.

Downloaded from https://academic.oup.com/imamat/advance-article/doi/10.1093/imamat/hxab025/6318163 by University of California, Berkeley user on 12 July 2021

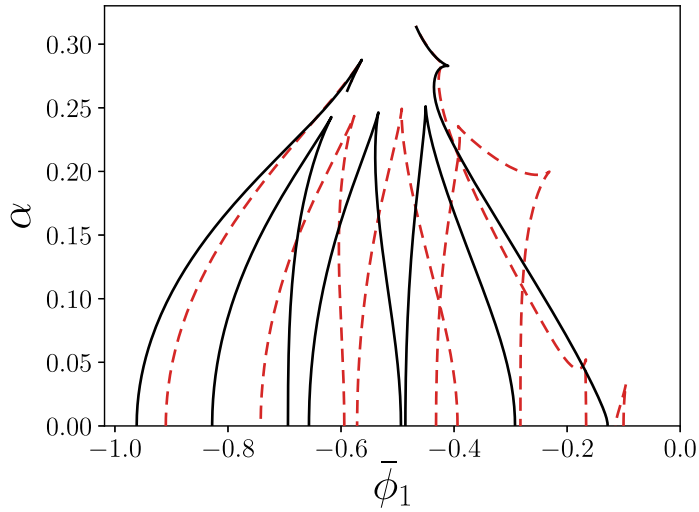

FIG. 12. For the coupled active and passive PFC model [Eqs. (5.1)] we show the loci in the $(\bar{\phi}_1, \alpha)$ plane of saddle-node bifurcations on the branches of resting symmetric localized states with even (dashed red lines) and odd (solid black lines) numbers of peaks. The remaining parameters are $r = -1.5$, $\bar{\phi}_2 = -2$ and $c = -0.2$.

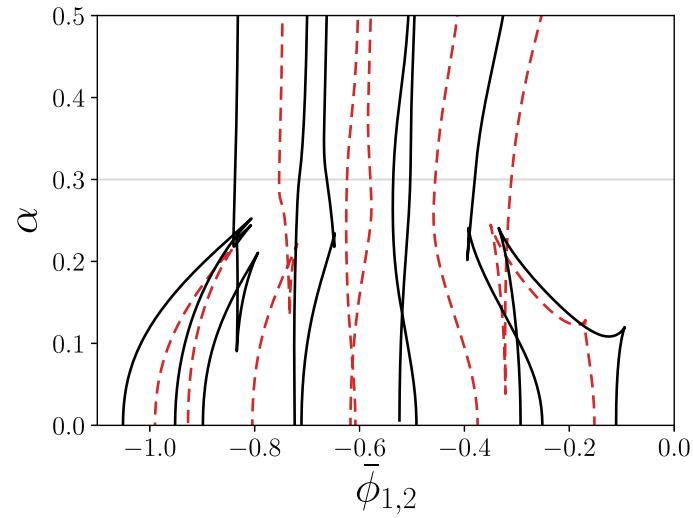

FIG. 13. For the coupled active and passive PFC model [Eqs. (5.1)] we show the loci in the $(\bar{\phi}, \alpha)$ plane of saddle-node bifurcations on the branches of resting symmetric localized states with even (dashed red lines) and odd (solid black lines) numbers of peaks, where $\bar{\phi} = \bar{\phi}_1 = \bar{\phi}_2$. Here $r = -1.5$ and the remaining parameters are as in Fig. 8. The horizontal line indicates the value of α for the bifurcation diagram in Fig. 14.

The loci of the saddle-node bifurcations along the diagonal $\bar{\phi} = \bar{\phi}_1 = \bar{\phi}_2$ are presented in Fig. 13. Here, only a minority of saddle-node bifurcations annihilate with increasing α. The majority continue to exist for large α and their loci in Fig. 13 become nearly vertical. This behavior can be understood noting that α plays the role of a 'nonequilibrium effective temperature', as discussed for the active PFC model

Downloaded from https://academic.oup.com/imamat/advance-article/doi/10.1093/imamat/hxab025/6318163 by University of California, Berkeley user on 12 July 2021

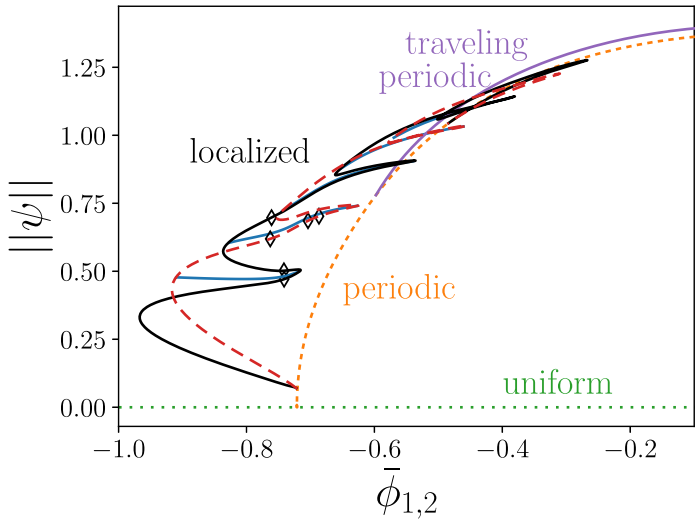

FIG. 14. Typical bifurcation diagram for the coupled active and passive PFC model [Eqs. (5.1)] corresponding to a horizontal cut at fixed $\alpha = 0.3$ through Fig. 13. Line styles are as in Fig. 8 while the remaining parameters are as in Fig. 13. The solid purple line corresponds to steadily traveling periodic states. The black diamonds indicate the locations of the first three Hopf bifurcations on the two branches of symmetric localized states.

in section 3. Since only ψ_1 (but not ψ_2) describes an active colloid, only the ψ_1-crystallites are affected by the 'effective temperature' influence of the activity α and melt as it increases, see Figs. 6 and 12. In contrast, the crystalline structure in ψ_2 persists. In fact, the influence of ψ_1 and (indirectly) P on these crystallites diminishes for large α because $\psi_1 \to 0$ and $P \to 0$ as α increases.

This observation is further illustrated in Fig. 14 where we present a bifurcation diagram along a horizontal cut through Fig. 13 at fixed $\alpha = 0.3$, i.e. above all the cusps. Here slanted snaking is still present, but for smaller $|\bar{\phi}_{1,2}|$, all states are destabilized by many Hopf bifurcations. The branches emerging there are not studied here but promise very rich behavior that is worth investigating. Of the localized states, only those on the lowest snaking branches are stable. These consist of one, two or three peaks of ψ_2, while the peaks of ψ_1 are initially suppressed and only appear further up on the snaking structure. However, the associated localized states are never stable as each branch of localized states undergoes a series of more than 30 destabilizing Hopf bifurcations. The first three of these on each branch are indicated in Fig. 14 by diamonds. In addition to the states present in Fig. 8, we also include the branch of steadily traveling periodic states.

6. Conclusions

We have explored the occurrence of slanted homoclinic snaking of localized states in a number of passive and active PFC models. The standard one-field PFC model (Elder & Grant, 2004; Emmerich *et al.*, 2012) corresponds to the conserved SH equation and is perhaps the simplest example of a pattern-forming system with a conserved quantity. The bifurcation structure involving snaking branches of localized states is analysed in detail by Thiele *et al.* (2013) and was reviewed here and extended, focusing on 1D systems. The main features are the occurrence of localized states even when the branch of periodic states bifurcates supercritically from the uniform state, strongly subcritical bifurcations generating

Downloaded from https://academic.oup.com/imamat/advance-article/doi/10.1093/imamat/hxab025/6318163 by University of California, Berkeley user on 12 July 2021

Downloaded from https://academic.oup.com/imamat/advance-article/doi/10.1093/imamat/hxab025/6318163 by University of California, Berkeley user on 12 July 2021

spatially localized states that may exist even outside the two-phase coexistence region between the uniform (liquid) state and the periodic (crystal) state, organization of these states into a slanted snakes-and-ladders structure and a transition from slanted snaking to smooth snaking when the effective temperature is increased. In the latter case, the localized states grow smoothly in size as the mean density increases without specific nucleation events. In fact, all these are properties of conserved systems *in general* (Knobloch, 2016). Moreover, stability still changes along the localized state branches owing to the continued existence of rung branches of asymmetric states. These properties are intrinsically related to the redistribution of the conserved density between patterned and uniform regions, i.e. it is a finite size effect. For an analysis of the transition from finite-domain bifurcation diagrams to the Maxwell construction of the thermodynamics of first-order phase transitions in 1D and 2D, see Thiele *et al.* (2019). We have also explained how slanted snaking turns into aligned snaking when the data is presented over a different control parameter and have pointed out the resulting intricacies in the interpretation of the bifurcation diagram. These points are further elaborated in the conclusion of Thiele *et al.* (2013). Related connections between steady solutions of conserved and nonconserved variants of other models, namely, Allen–Cahn vs. Cahn–Hilliard model and SH vs. PFC model, are discussed by Engelnkemper *et al.* (2019).

We have also considered the active PFC model of Menzel & Löwen (2013) where the concentration field is coupled to a polarization field in a manner that breaks the gradient dynamics form of the model, i.e. renders it 'active'. We have summarized and expanded on the main results of Ophaus *et al.* (2018) for this model. In particular, we have illustrated how the slanted homoclinic snaking structure of the PFC case is amended by activity and showed that increasing activity beyond certain threshold values leads on the one hand to the melting of the various resting localized states and on the other hand to the onset of drift. Using the activity parameter as the main control parameter we explained that traveling localized states emerge either via drift-pitchfork bifurcations of steady symmetric localized states or via drift-transcritical bifurcations of steady asymmetric localized states. This is a particular feature of the active PFC model that has not yet, to our knowledge, been remarked upon. The onset behavior we find differs from that in the nonvariational SH equation considered by Houghton & Knobloch (2011). There, all asymmetric states drift for any nonzero activity. The details of the onset behavior in the systems studied here, the various traveling states and their interactions are further discussed by Ophaus *et al.* (2018) and Ophaus *et al.* (2020) with the 2D case considered by Ophaus *et al.* (2021). We have also pointed out that the bifurcation structure describing dissolution of crystallites with increasing activity resembles that obtained on increasing the effective temperature in the passive case. This implies that melting of passive crystals can occur either via increasing temperature or via increasing activity, i.e. active motion of the constituents.

Next, we have considered a two-field PFC model for a crystallizing binary mixture, e.g. of two species of colloids, first with a variational coupling as in Holl *et al.* (2021b) and then with a nonvariational coupling. In the variational case the system allows for various liquid and crystalline phases and we have explored the occurrence of localized states in the vicinity of first-order phase transitions between the uniform (liquid) phase and a periodic (crystalline) alloy phase on the one hand, and a single-species crystalline phase and the crystalline alloy phase on the other. In both cases slanted snaking of localized states occurs and in fact represents a signature of the phase transition in the bifurcation diagrams for finite size domains. Here, we believe that a systematic study of bifurcation diagrams in the context of phase transitions may be useful for obtaining a deeper understanding of complex phase behavior in finite size systems. In this connection one may wonder whether the observed slanted snaking in the variational two-field PFC model can be straightened out in a similar way to that discussed in the one-field case. We believe that this should be possible but will not be straightforward

because the tie lines in Fig. 7 are not lines of fixed $\bar{\phi}_1$ or $\bar{\phi}_2$. However, one could consider the bifurcation structure in higher dimensional space following the representation in Fig. 7 but plotting $\bar{\phi}_1$ and $\bar{\phi}_2$ over μ_1 and μ_2. The results may be difficult to visualize, however, since the bifurcation structure would not consist of curves but of surfaces.

The variational case serves as a reference for the two-field PFC model with a nonvariational coupling. The chosen coupling respects both conservation laws, i.e. it does not represent a chemical reaction between components and can be seen as a continuous predator–prey-type model of two potentially crystallizing species: e.g. for positive nonvariational coupling α in Eqs. (4.1) species 1 would be repelled by species 2 while species 2 is attracted by species 1, not unlike the attraction–repulsion set-up by Burger *et al.* (2014) and Chen & Kolokolnikov (2014). Recently, such couplings have also been studied for active two-field Cahn–Hilliard-type models (Frohoff-Hülsmann *et al.*, 2021; Saha *et al.*, 2020; You *et al.*, 2020); for localized states in such models, see Frohoff-Hülsmann & Thiele (2021) in the present volume.

Here, we have considered how activity affects homoclinic snaking in this type of two-field PFC model and have found that it acts much like the effective temperature in passive PFC models. However, depending on the sign of the active coupling, the 'destruction' of the snaking structure with increasing activity changes. We have not explored the emergence of traveling and oscillating states but mention that such states occur in this system and promise rich bifurcation behavior that awaits exploration.

Finally, we have briefly analyzed another active PFC model for a binary mixture of a passive and an active colloid species as studied experimentally, e.g. by Bechinger *et al.* (2016). Here we have coupled a passive single-species PFC model with an active single-species PFC model. Our analysis showed that depending on the type of underlying phase transition considered, snaking branches of localized states may or may not be destroyed by increasing the activity. Note also that in this model activity results in the emergence of traveling states that are not considered here.

Overall we have found that all the PFC systems considered here exhibit slanted snakes-and-ladders structures of intertwined branches of symmetric localized states connected by branches of asymmetric localized states. In the variational case, i.e. for gradient dynamics, the homoclinic snaking structure is always an expression of an underlying first-order phase transition and can be used to identify its equivalent for systems of finite size. In this case, by definition, all states are at rest. For the one-field PFC model the transition from slanted homoclinic snaking to the thermodynamic Maxwell construction is considered by Thiele *et al.* (2019). However, for the passive two-field PFC model where also three-phase coexistence occurs (Holl *et al.*, 2021b) this type of analysis is more intricate and remains to be done.

All the active models considered here are intrinsically out-of-equilibrium models as they feature nonreciprocal interactions (Ivlev *et al.*, 2015) between the fields. As activity is increased from zero the entire slanted snake-and-ladder branch structure of resting localized states remains at first qualitatively unchanged. In all the cases, increasing activity influenced the subsequent bifurcation structure in a similar way to increasing the effective temperature in the passive case. This was already remarked on by Menzel & Löwen (2013) when considering the occurrence of periodic crystalline structures in the one-field PFC model. For the symmetric localized states their existence as resting states is expected. However, the universal existence of resting asymmetric localized states in all three active models is unexpected and will be explained in a forthcoming publication.

In the present work we have focused on steady states and have mentioned traveling and oscillating localized states only in passing. As one increases the activity beyond threshold values such time-dependent states occur in all the active models considered here. For the one-species active PFC model, the occurrence of drift bifurcations is studied by Ophaus *et al.* (2018) and Ophaus *et al.* (2021), and

Downloaded from https://academic.oup.com/imamat/advance-article/doi/10.1093/imamat/hxab025/6318163 by University of California, Berkeley user on 12 July 2021

some oscillatory states are described by Ophaus *et al.* (2020). However, the emergence and interplay of drift and Hopf bifurcations along the snakes-and-ladders structure awaits more detailed studies.

Acknowledgements

All authors thank the Center of Nonlinear Science (CeNoS) of the University of Münster for support of their collaboration.

Funding

Franco-German University (CDFA-01-14 to U.T., L.O. and M.H.); National Science Foundation (DMS-1908891 to E.K.).

References

Avitabile, D., Lloyd, D. J. B., Burke, J., Knobloch, E. & Sandstede, B. (2010) To snake or not to snake in the planar Swift–Hohenberg equation. *SIAM J. Appl. Dyn. Syst.*, **9**, 704–733.

Ball, P. (1999) *The Self-Made Tapestry: Pattern Formation in Nature*. Oxford: Oxford University Press.

Barten, W., Lücke, M. & Kamps, M. (1991) Localized traveling-wave convection in binary-fluid mixtures. *Phys. Rev. Lett.*, **66**, 2621–2624.

Bechinger, C., Di Leonardo, R., Löwen, H., Reichhardt, C., Volpe, G. & Volpe, G. (2016) Active particles in complex and crowded environments. *Rev. Mod. Phys*, **88**, 045006.

Bordeu, I., Clerc, M. G., Couteron, P., Lefever, R. & Tlidi, M. (2016) Self-replication of localized vegetation patches in scarce environments. *Sci. Rep.*, **6**, 33703.

Bortolozzo, U., Clerc, M. G. & Residori, S. (2008) Local theory of the slanted homoclinic snaking bifurcation diagram. *Phys. Rev. E*, **78**, 036214.

Burger, M., Fetecau, R. & Huang, Y. H. (2014) Stationary states and asymptotic behavior of aggregation models with nonlinear local repulsion. *SIAM J. Appl. Dyn. Syst.*, **13**, 397–424.

Burke, J. & Dawes, J. H. P. (2012) Localized states in an extended Swift–Hohenberg equation. *SIAM J. Appl. Dyn. Syst.*, **11**, 261–284.

Burke, J., Houghton, S. M. & Knobloch, E. (2009) Swift–Hohenberg equation with broken reflection symmetry. *Phys. Rev. E*, **80**, 036202.

Burke, J. & Knobloch, E. (2006) Localized states in the generalized Swift–Hohenberg equation. *Phys. Rev. E*, **73**, 056211.

Burke, J. & Knobloch, E. (2007) Snakes and ladders: localized states in the Swift–Hohenberg equation. *Phys. Lett. A*, **360**, 681–688.

Chen, Y. X. & Kolokolnikov, T. (2014) A minimal model of predator-swarm interactions. *J. R. Soc. Interface*, **11**, 20131208.

Chervanyov, A. I., Gomez, H. & Thiele, U. (2016) Effect of the orientational relaxation on the collective motion of patterns formed by self-propelled particles. *Europhys. Lett.*, **115**, 68001.

Cox, S. M. (2004) The envelope of a one-dimensional pattern in the presence of a conserved quantity. *Phys. Lett. A*, **333**, 91–101.

Cox, S. M. & Matthews, P. C. (2003) Instability and localisation of patterns due to a conserved quantity. *Phys. D*, **175**, 196–219.

Cross, M. & Greenside, H. (2009) *Pattern Formation and Dynamics in Nonequilibrium Systems*. Cambridge, UK; New York: Cambridge University Press.

Cross, M. C. & Hohenberg, P. C. (1993) Pattern formation out of equilibrium. *Rev. Mod. Phys.*, **65**, 851–1112.

Dawes, J. H. P. (2008) Localized pattern formation with a large-scale mode: slanted snaking. *SIAM J. Appl. Dyn. Syst.*, **7**, 186–206.

Downloaded from https://academic.oup.com/imamat/advance-article/doi/10.1093/imamat/hxab025/6318163 by University of California, Berkeley user on 12 July 2021

Doedel, E., Keller, H. B. & Kernevez, J. P. (1991) Numerical analysis and control of bifurcation problems (I): bifurcation in finite dimensions. *Int. J. Bifurcation Chaos*, **1**, 493–520.

Elder, K. R. & Grant, M. (2004) Modeling elastic and plastic deformations in nonequilibrium processing using phase field crystals. *Phys. Rev. E*, **70**, 051605.

Elder, K. R., Katakowski, M., Haataja, M. & Grant, M. (2002) Modeling elasticity in crystal growth. *Phys. Rev. Lett.*, **88**, 245701.

Emmerich, H., Löwen, H., Wittkowski, R., Gruhn, T., Tóth, G. I., Tegze, G. & Gránásy, L. (2012) Phase-field-crystal models for condensed matter dynamics on atomic length and diffusive time scales: an overview. *Adv. Phys.*, **61**, 665–743.

Engelnkemper, S., Gurevich, S. V., Uecker, H., Wetzel, D. & Thiele, U. (2019) Continuation for thin film hydrodynamics and related scalar problems. In: Gelfgat A. (ed) *Computational Modelling of Bifurcations and Instabilities in Fluid Dynamics*. Computational Methods in Applied Sciences. vol. **50**, pp. 459–501.

Frohoff-Hülsmann, T. & Thiele, U. (2021) Localised states in coupled Cahn–Hilliard equations. (submitted, preprint at arxiv: http://arxiv.org/abs/2010.14183). doi: https://doi.org/10.1093/imamat/hxab026

Frohoff-Hülsmann, T., Wrembel, J. & Thiele, U. (2021) Suppression of coarsening and emergence of oscillatory behavior in a Cahn–Hilliard model with nonvariational coupling. *Phys. Rev. E*, **103**, 042602. Corresponding data can be found on zenodo under http://doi.org/10.5281/zenodo.4275309.

Ginot, F., Theurkauff, I., Detcheverry, F., Ybert, C. & Cottin-Bizonne, C. (2018) Aggregation–fragmentation and individual dynamics of active clusters. *Nat. Commun.*, **9**, 696.

Hariz, A., Bahloul, L., Cherbi, L., Panajotov, K., Clerc, M., Ferré, M. A., Kostet, B., Averlant, E. & Tlidi, M. (2019) Swift–Hohenberg equation with third-order dispersion for optical fiber resonators. *Phys. Rev. A*, **100**, 023816.

Hilali, M. F., Métens, S., Borckmans, P. & Dewel, G. (1995) Pattern selection in the generalized Swift–Hohenberg model. *Phys. Rev. E*, **51**, 2046–2052.

Holl, M. P., Archer, A., Gurevich, S. V., Knobloch, E., Ophaus, L. & Thiele, U. (2021a) *Data Supplement for 'Localized States in Passive and Active Phase-Field-Crystal Models'*. Available at https://doi.org/10.5281/zenodo.4795157.

Holl, M. P., Archer, A. J. & Thiele, U. (2021b) Efficient calculation of phase coexistence and phase diagrams: application to a binary phase-field crystal model. *J. Phys. Condens. Matter*, **33**, 115401. Corresponding data and computer codes can be found on zenodo under http://doi.org/10.5281/zenodo.4269554.

Houghton, S. M. & Knobloch, E. (2011) Swift–Hohenberg equation with broken cubic-quintic nonlinearity. *Phys. Rev. E*, **84**, 016204.

Hoyle, R. B. (2006) *Pattern Formation—An Introduction to Methods*. Cambridge: Cambridge University Press.

Hunt, G. W., Peletier, M. A., Champneys, A. R., Woods, P. D., Ahmer Wadee, M., Budd, C. J. & Lord, G. J. (2000) Cellular buckling in long structures. *Nonlinear Dyn.*, **21**, 3–29.

Ivlev, A. V., Bartnick, J., Heinen, M., Du, C. R., Nosenko, V. & Löwen, H. (2015) Statistical mechanics where Newton's third law is broken. *Phys. Rev. X*, **5**, 011035.

Knobloch, E. (2015) Spatial localization in dissipative systems. *Annu. Rev. Condens. Matter Phys.*, **6**, 325–359.

Knobloch, E. (2016) Localized structures and front propagation in systems with a conservation law. *IMA J. Appl. Math.*, **81**, 457–487.

Knobloch, E., Uecker, H. & Wetzel, D. (2019) Defectlike structures and localized patterns in the cubic-quintic-septic Swift–Hohenberg equation. *Phys. Rev. E*, **100**, 012204.

Kozyreff, G., Assemat, P. & Chapman, S. J. (2009) Influence of boundaries on localized patterns. *Phys. Rev. Lett.*, **103**, 164501.

Kozyreff, G. & Chapman, S. J. (2006) Asymptotics of large bound states of localized structures. *Phys. Rev. Lett.*, **97**, 044502.

Kozyreff, G. & Tlidi, M. (2007) Nonvariational real Swift–Hohenberg equation for biological, chemical, and optical systems. *Chaos*, **17**, 037103.

Krauskopf, B., Osinga, H. M. & Galan-Vioque, J. (eds.) (2007) *Numerical Continuation Methods for Dynamical Systems*. Dordrecht: Springer.

Downloaded from https://academic.oup.com/imamat/advance-article/doi/10.1093/imamat/hxab025/6318163 by University of California, Berkeley user on 12 July 2021

Kubstrup, C., Herrero, H. & PerezGarcia, C. (1996) Fronts between hexagons and squares in a generalized Swift–Hohenberg equation. *Phys. Rev. E*, **54**, 1560–1569.

Lejeune, O., Tlidi, M. & Lefever, R. (2004) Vegetation spots and stripes: dissipative structures in arid landscapes. *Int. J. Quantum Chem.*, **98**, 261–271.

Lloyd, D. & Sandstede, B. (2009) Localized radial solutions of the Swift–Hohenberg equation. *Nonlinearity*, **22**, 485–524.

Lloyd, D. J. B., Gollwitzer, C., Rehberg, I. & Richter, R. (2015) Homoclinic snaking near the surface instability of a polarisable fluid. *J. Fluid Mech.*, **783**, 283–305.

Lloyd, D. J. B., Sandstede, B., Avitabile, D. & Champneys, A. R. (2008) Localized hexagon patterns of the planar Swift–Hohenberg equation. *SIAM J. Appl. Dyn. Syst.*, **7**, 1049–1100.

Lo Jacono, D., Bergeon, A. & Knobloch, E. (2011) Magnetohydrodynamic convectons. *J. Fluid Mech*, **687**, 595–605.

Marchetti, M. C., Joanny, J. F., Ramaswamy, S., Liverpool, T. B., Prost, J., Rao, M. & Simha, R. A. (2013) Hydrodynamics of soft active matter. *Rev. Mod. Phys.*, **85**, 1143–1189.

Matthews, P. C. & Cox, S. M. (2000) Pattern formation with a conservation law. *Nonlinearity*, **13**, 1293–1320.

McCalla, S. & Sandstede, B. (2010) Snaking of radial solutions of the multi-dimensional Swift–Hohenberg equation: a numerical study. *Phys. D*, **239**, 1581–1592.

Menzel, A. M. & Löwen, H. (2013) Traveling and resting crystals in active systems. *Phys. Rev. Lett.*, **110**, 055702.

Menzel, A. M., Ohta, T. & Löwen, H. (2014) Active crystals and their stability. *Phys. Rev. E*, **89**, 022301.

Ophaus, L., Gurevich, S. V. & Thiele, U. (2018) Resting and traveling localized states in an active phase-field-crystal model. *Phys. Rev. E*, **98**, 022608.

Ophaus, L., Kirchner, J., Gurevich, S. V. & Thiele, U. (2020) Phase-field-crystal description of active crystallites: elastic and inelastic collisions. *Chaos*, **30**, 123149. Corresponding data can be found on zenodo under http://doi.org/10.5281/zenodo.4322991.

Ophaus, L., Knobloch, E., Gurevich, S. V. & Thiele, U. (2021) Two-dimensional localized states in an active phase-field-crystal model. *Phys. Rev. E*, **103**, 032601. Corresponding data can be found on zenodo under http://doi.org/10.5281/zenodo.4554733.

Ouchi, K. & Fujisaka, H. (1996) Phase ordering kinetics in the Swift–Hohenberg equation. *Phys. Rev. E*, **54**, 3895–3898.

Palacci, J., Sacanna, S., Steinberg, A. P., Pine, D. J. & Chaikin, P. M. (2013) Living crystals of light-activated colloidal surfers. *Science*, **339**, 936–940.

Petroff, A. P., Wu, X.-L. & Libchaber, A. (2015) Fast-moving bacteria self-organize into active two-dimensional crystals of rotating cells. *Phys. Rev. Lett.*, **114**, 158102.

Pismen, L. M. (2006) *Patterns and Interfaces in Dissipative Dynamics*. Berlin Heidelberg: Springer.

Pradenas, B., Araya, I., Clerc, M. G., Falcon, C., Gandhi, P. & Knobloch, E. (2017) Slanted snaking of localized Faraday waves. *Phys. Rev. Fluids*, **2**, 064401.

Robbins, M. J., Archer, A. J., Thiele, U. & Knobloch, E. (2012) Modelling the structure of liquids and crystals using one- and two-component modified phase-field crystal models. *Phys. Rev. E*, **85**, 061408.

Saha, S., Agudo-Canalejo, J. & Golestanian, R. (2020) Scalar active mixtures: the non-reciprocal Cahn–Hilliard model. *Phys. Rev. X*, **10**, 041009.

Sakaguchi, H. & Brand, H. R. (1996) Stable localized solutions of arbitrary length for the quintic Swift–Hohenberg equation. *Phys. D*, **97**, 274–285.

Surko, C. M., Ohlsen, D. R., Yamamoto, S. Y. & Kolodner, P. (1991) Confined states of traveling-wave convection. *Phys. Rev. A*, **43**, 7101–7104.

Tegze, G., Gránásy, L., Tóth, G. I., Podmaniczky, F., Jaatinen, A., Ala-Nissila, T. & Pusztai, T. (2009) Diffusion-controlled anisotropic growth of stable and metastable crystal polymorphs in the phase-field crystal model. *Phys. Rev. Lett.*, **103**, 035702.

Thar, R. & Kühl, M. (2005) Complex pattern formation of marine gradient bacteria explained by a simple computer model. *FEMS Microbiol. Lett.*, **246**, 75–79.

Downloaded from https://academic.oup.com/imamat/advance-article/doi/10.1093/imamat/hxab025/6318163 by University of California, Berkeley user on 12 July 2021

Theurkauff, I., Cottin-Bizonne, C., Palacci, J., Ybert, C. & Bocquet, L. (2012) Dynamic clustering in active colloidal suspensions with chemical signaling. *Phys. Rev. Lett.*, **108**, 268303.

Thiele, U., Archer, A. J., Robbins, M. J., Gomez, H. & Knobloch, E. (2013) Localized states in the conserved Swift–Hohenberg equation with cubic nonlinearity. *Phys. Rev. E*, **87**, 042915. Corresponding data can be found on zenodo under http://doi.org/10.5281/zenodo.3890105.

Thiele, U., Frohoff-Hülsmann, T., Engelnkemper, S., Knobloch, E. & Archer, A. J. (2019) First order phase transitions and the thermodynamic limit. *New J. Phys.*, **21**, 123021.

Tlidi, M., Mandel, P. & Lefever, R. (1994) Localized structures and localized patterns in optical bistability. *Phys. Rev. Lett.*, **73**, 640–643.

Toner, J. & Tu, Y. (1995) Long-range order in a 2-dimensional dynamical xy model—how birds fly together. *Phys. Rev. Lett.*, **75**, 4326–4329.

Toner, J., Tu, Y. & Ramaswamy, S. (2005) Hydrodynamics and phases of flocks. *Ann. Phys.*, **318**, 170–244.

Uecker, H., Wetzel, D. & Rademacher, J. D. M. (2014) pde2path—a Matlab package for continuation and bifurcation in 2D elliptic systems. *Numer. Math. Theory Methods Appl.*, **7**, 58–106.

Umbanhowar, P. B., Melo, F. & Swinney, H. L. (1996) Localized excitations in a vertically vibrated granular layer. *Nature*, **382**, 793–796.

van Teeffelen, S., Backofen, R., Voigt, A. & Löwen, H. (2009) Derivation of the phase-field-crystal model for colloidal solidification. *Phys. Rev. E*, **79**, 051404.

Woods, P. D. & Champneys, A. R. (1999) Heteroclinic tangles and homoclinic snaking in the unfolding of a degenerate reversible Hamiltonian–Hopf bifurcation. *Phys. D*, **129**, 147–170.

You, Z. H., Baskaran, A. & Marchetti, M. C. (2020) Nonreciprocity as a generic route to traveling states. *Proc. Natl. Acad. Sci. U. S. A.*, **117**, 19767–19772.

Downloaded from https://academic.oup.com/imamat/advance-article/doi/10.1093/imamat/hxab025/6318163 by University of California, Berkeley user on 12 July 2021